



Thermal Pressurization and Onset of Melting in Fault Zones

Citation

Rempel, Alan W. and James R. Rice. 2006. Thermal pressurization and onset of melting in fault zones. *Journal of Geophysical Research* 111:B09314.

Published Version

doi:10.1029/2006JB004314

Permanent link

<http://nrs.harvard.edu/urn-3:HUL.InstRepos:5029990>

Terms of Use

This article was downloaded from Harvard University's DASH repository, and is made available under the terms and conditions applicable to Other Posted Material, as set forth at <http://nrs.harvard.edu/urn-3:HUL.InstRepos:dash.current.terms-of-use#LAA>

Share Your Story

The Harvard community has made this article openly available. Please share how this access benefits you. [Submit a story](#).

[Accessibility](#)



Thermal pressurization and onset of melting in fault zones

Alan W. Rempel¹ and James R. Rice²

Received 28 January 2006; revised 27 May 2006; accepted 7 June 2006; published 23 September 2006.

[1] We examine how frictional heating drives the evolution of temperature, strength, and fracture energy during earthquake slip. For small slip distances, heat and pore fluid are unable to escape the shearing fault core, and the behavior is well approximated by simple analytical models that neglect any transport. Following large slip distances, the finite width of the shear zone is small compared to the thicknesses of the thermal and hydrological boundary layers, and the fault behavior approaches that predicted for the idealized case of slip on a plane. To evaluate the range in which the predictions of these two sets of approximations are valid, we develop a model that describes how frictional dissipation within a finite shear zone drives heat and mass transport through the surrounding static gouge. With realistic parameter values and slips greater than a few centimeters, the subsequent evolution of strength and fracture energy are approximated well by the planar slip model. However, the temperature evolution is much more sensitive to the finite shear zone thickness, and the ultimate temperature rise tends to be intermediate between that predicted for the two simplified cases. We explore the range of conditions necessary for melting to begin and focus in particular on the potential role of fault zone damage in facilitating fluid transport and promoting larger temperature increases. We discuss how the apparent scarcity of exhumed pseudotachylytes places constraints on some of the more uncertain fault zone parameters.

Citation: Rempel, A. W., and J. R. Rice (2006), Thermal pressurization and onset of melting in fault zones, *J. Geophys. Res.*, *111*, B09314, doi:10.1029/2006JB004314.

1. Introduction

[2] The energy radiated during earthquakes carries immense destructive power. Yet this is only a single component of the seismic energy balance. Following the high-speed passage of the rupture front, we expect much of the energy released during shear to be converted to heat. Such reasoning prompted early scaling arguments which suggested that the heat released during earthquakes should often cause large volumes of the nearby fault rocks to melt [e.g., *Jeffreys*, 1942; *McKenzie and Brune*, 1972]. The scarcity of geologic evidence for widespread frictional melting led *Sibson* [1973] to argue that the pressurization of pore fluids housed in the granular fault gouge could reduce fault strength during seismic shear, thereby limiting the temperature rise. Noting the absence of a clear temperature anomaly near the San Andreas fault [*Lachenbruch and Sass*, 1980], an observation now referred to as the “heat flow paradox,” *Lachenbruch* [1980] developed a simple model to quantify how thermal pressurization might operate. Subsequent model developments [*Mase and Smith*, 1985, 1987; *Andrews*, 2002; *Rice*,

2006; *Rice and Cocco*, 2006] have further demonstrated that the relatively large thermal expansion coefficient of water in comparison to those of the fault gouge solids can lead to enhanced pore pressures that reduce fault strength during seismic slip.

[3] Refinements to our understanding of fault zone behavior, based on recent field and laboratory results, make it possible to reassess and better constrain the effects of thermal pressurization. In particular, the field observations suggest that the shear zone is much more localized than had been commonly believed, with most of the slip occurring within a thin shear zone, typically <1–5 mm thick, which itself lies within a highly granulated “ultracataclastic” layer that may be of order 10–100 mm broad [*Chester and Chester*, 1998; *Lockner et al.*, 2000; *Chester et al.*, 2004; *Wibberly and Shimamoto*, 2003; *Sibson*, 2003; *Noda and Shimamoto*, 2005]. This is comparable in thickness to the thermal and hydrological boundary layers that characterize heat and fluid transport during shear. In fact, close examination of crystallographic preferred orientations within a millimeter-thick shear zone along the Punchbowl fault point to much more extreme localization; most of the slip may actually be confined to a zone with an apparent thickness of only 0.1–0.3 mm [*Chester et al.*, 2003; *Chester and Goldsby*, 2003]. As discussed further by *Rice* [2006], studies of shear banding in granular media typically find that most deformation is concentrated within layers of order 10–100 particle diameters in width. Analysis of the Punchbowl fault ultracataclastic, which hosts the localized shear zone,

¹Department of Geological Sciences, University of Oregon, Eugene, Oregon, USA.

²Department of Earth and Planetary Sciences, and Division of Engineering and Applied Sciences, Harvard University, Cambridge, Massachusetts, USA.

reveals a broad distribution of particle sizes, with approximately 50% by weight smaller than $1\ \mu\text{m}$ in diameter [Chester *et al.*, 2005], so shear zone thicknesses of order 0.1 mm are consistent with expectations. Wibberley and Shimamoto [2005] have introduced the assumption that the entire thickness of the ultracataclastic zone undergoes seismic shear during earthquakes, thus suggesting much greater slip zone thicknesses of up to several tens of millimeters based on observations of gouge from the Median Tectonic Line (MTL) in Japan. However, their own report of MTL fault core structures [Wibberley and Shimamoto, 2003, Figure 11] suggests that concentrated slip may occur within a much thinner zone, reported to have a nominal thickness of $\sim 3\ \text{mm}$ (C. A. Wibberley, private communication, 2003). The assumption of a wide shear zone enabled them to use an elementary thermal pressurization model, with effectively adiabatic and undrained deformation on the seismic timescale, to infer slip-weakening distances and fracture energies that are thought to be representative of large earthquakes. Assumption of a broad shear zone is not necessary to the result; Rice [2006] and the present work shows that the earthquake data set for fracture energies can be fit to predictions of a model involving slip on a much thinner zone, even slip on a mathematical plane. It is, nevertheless, presently uncertain whether broad zones of ultracataclastic gouge, up to several tens of millimeters width, participate in seismic shear, or whether extreme localization is the rule even if such localized zones may have in some cases evaded detection. An expanded theoretical discussion of the balances that determine the shear zone thickness is contained within a manuscript currently in preparation by J. R. Rice and J. W. Rudnicki (Stability of spatially uniform, adiabatic, undrained shear of a fault zone, manuscript in preparation, 2006) [see also Rice *et al.*, 2005]; results, based on present understanding of material parameter choices for the ultracataclastic argue for millimeter to submillimeter scales of shear zone thickness.

[4] Laboratory experiments are beginning to achieve both high slip rates and long slip distances at confining stresses that are characteristic of shallow seismogenic depths. One clear result is the observation that the effective friction coefficient under these conditions is much lower than that which is more commonly manifest under less extreme conditions (e.g., lower slip rates, low confining stress) [Tsutsumi and Shimamoto, 1997; Tullis and Goldsby, 2003a, 2003b; Prakash, 2004; Prakash and Yuan, 2004; V. Prakash and F. Yuan, private communication, November 2004]. In some cases weakening is associated with the formation of silica gels that effectively lubricate the contact zone [Goldsby and Tullis, 2002; Di Toro *et al.*, 2004; Roig Silva *et al.*, 2004]. However, this mechanism cannot explain the weakening observed in friction experiments that use rocks with low silica contents. Instead, drawing on the long-standing explanation for high-speed frictional behavior in metals [e.g., Bowden and Thomas, 1954], Rice [1999] proposed that localized heating and weakening at asperity contacts could be responsible. This “flash-weakening” mechanism has since been developed further [Rice, 2006; N. M. Beeler and T. E. Tullis, Constitutive relationships for fault strength due to flash heating, submitted to *U.S. Geological Survey Open File Report*, 2003] and we make reference to it in choosing a nominal friction coefficient for

use in the calculations that follow. A few laboratory studies have focused on the complex changes in frictional behavior following the onset of bulk melting [Tsutsumi and Shimamoto, 1997; Hirose and Shimamoto, 2005]. We note, however, that no experimental configuration has yet been successful at directly testing the mechanism of thermal pressurization itself.

[5] Here, we extend the analysis of Rice [2006] to describe the role of pore fluids in controlling the evolution of fault strength and temperature during the distributed shear of a thin, fluid-saturated gouge layer. We begin in section 2 by describing an elementary kinematic model and outlining a set of representative parameters that are used to characterize the behavior of a mature fault zone during seismic shear. In section 3, we describe how the fault is expected to behave under two sets of limiting circumstances: one that characterizes the evolution at early times, when the transport of heat and mass have negligible effect, and one that characterizes late time evolution, when the shear zone thickness is small in comparison to the thickness of the thermal and hydrological boundary layers. Numerical solutions for the evolution of temperature and pore pressure during distributed shear are presented in section 4. We focus primarily on the case where shear is uniform in a zone of prescribed thickness h . We examine how the system evolves between the two limiting cases discussed in section 3, then compare how the predictions change when the shear distribution is Gaussian, as proposed by Andrews [2002]. For both distributed shear models we find that once the slip achieves distances that characterize moderately large earthquakes, the fault strength and fracture energy are both well represented by the planar slip model. However, the temperature evolution is more sensitive to the effects of the finite fault width, so we next explore the model predictions to delineate parameter regimes under which melting can or cannot occur at a given seismogenic depth. Before concluding, in section 6 we examine briefly how state-dependent changes to the physical properties affect the predicted evolution of temperature and strength.

2. Model Description

[6] We develop a kinematic model for earthquake slip that is designed to probe the essential balances that define the characteristics of thermal pressurization. In future work these will be incorporated within fully dynamic calculations that include the effect of fault strength on slip rate. We do not explicitly treat the short-duration dynamics that perturb conditions as the rupture front propagates past a given point on the planar fault surface; instead, we view these changes only as setting the initial conditions from which the modeled state subsequently evolves. We treat the shear zone and surrounding stationary fault gouge as a fluid-saturated porous medium and we develop conservation conditions to describe how the temperature and pore pressure evolve in response to the mechanical work associated with earthquake slip. After carrying out the analysis to determine the system behavior for this idealized case, we discuss several model extensions that are aimed at assessing the influence of additional physical interactions, including those that arise from the state dependence of fault zone properties.

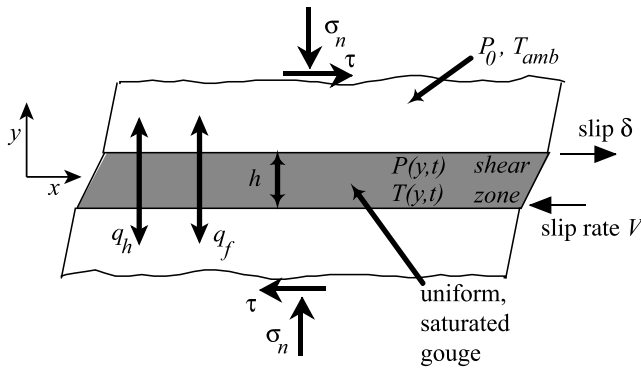


Figure 1. Schematic diagram of the fault zone. A layer of uniform, water-saturated gouge with thickness h shears at slip rate V , producing a temperature increase that causes the pore pressure to rise. The variations in shear zone conditions and the attendant evolution of fault shear strength are regulated by heat and fluid transport to the bounding, stationary gouge.

2.1. Conservation Conditions

[7] Consider a shear zone of thickness h that begins to undergo slip δ at time $t = 0$ with an imposed overall slip rate $V \equiv d\delta/dt$ in the x direction, as shown in Figure 1. The conservation conditions determine how the pore pressure and temperature evolve from their initial, uniform values P_0 and T_{amb} , which we designate as the “reference state”. The normal stress σ_n remains constant over the duration of slip. Consistent with the level of approximation used in the current work, in the following the frictional resistance is assumed to be proportional to the effective stress on the midplane, so that

$$\tau(t) = f(t)[\sigma_n - P(0, t)], \quad (1)$$

where $P(y, t)$ is the pore pressure and $f(t)$ is the coefficient of friction. The limitations of modeling the shear stress using a simple Coulomb friction model such as this are discussed in the appendix of Rice [2006]. The Lagrangian coordinate y marks positions of the solid gouge particles, measured perpendicular to the plane of the shear layer, in the reference state. We assume that all the work associated with shearing the gouge at rate $\dot{\gamma}$ is transformed into sensible heat. This produces a temperature increase, which is modulated by the effects of heat flow so that

$$\rho c \frac{\partial T}{\partial t} = -\frac{\partial q_h}{\partial y} + \tau \dot{\gamma}, \quad (2)$$

where ρc is the effective heat capacity per unit volume in the reference state. The outward flow of heat $q_h = -K\partial T/\partial y$ is treated as purely conductive and proportional to the effective conductivity K . The expenditure of energy required to create new surfaces as gouge particles break is not considered here (later, we comment on how to interpret the results if only a fraction of work is transformed, the rest appearing, e.g., as surface energy increase by granulation).

[8] We need to specify the shear distribution before proceeding further. To begin with we assume that the shear is uniform so that $\dot{\gamma} = V/h$, where we treat V as a constant in

the calculations that follow. Later we discuss how the results differ if we adopt the Gaussian distribution of shear rate proposed by Andrews [2002]. Substituting for $\dot{\gamma}$, q_h and τ , and treating the thermal diffusivity $\alpha_{th} \equiv K/\rho c$ as a constant for now, we write the temperature evolution in the shear layer $-h/2 \leq y \leq h/2$ as

$$\dot{T} = \alpha_{th} \frac{\partial^2 T}{\partial y^2} + f[\sigma_n - P(0, t)] \frac{V}{\rho c h}, \quad (3)$$

where $\dot{T} \equiv \partial T/\partial t$. Heat flowing out of the shear zone is conducted away so that the temperature for $|y| \geq h/2$ satisfies

$$\dot{T} = \alpha'_{th} \frac{\partial^2 T}{\partial y^2}. \quad (4)$$

Here, α'_{th} is the effective thermal diffusivity of the stationary gouge (e.g., for $|y| \geq h/2$). In the modeling that follows we focus on the special case where $\alpha'_{th} = \alpha_{th}$.

[9] Changes to the fluid mass within the shear zone are produced by outward advective transfer at mass flux q_f to the surrounding, static gouge. The fluid mass conservation condition is written as

$$\frac{\partial}{\partial t}(\rho_f n) = -\frac{\partial q_f}{\partial y}, \quad (5)$$

where ρ_f is the fluid density, and n is the ratio of the pore volume to the total volume in the reference state. Darcy’s law for fluid flow with viscosity η through gouge with permeability k gives $q_f = -(\rho_f k/\eta) \partial P/\partial y$, where $\partial P/\partial y$ is the deviation of the pressure gradient from hydrostatic equilibrium.

[10] We would like a second relationship between the evolution of the state variables P and T and their spatial gradients. To proceed, we substitute Darcy’s law into equation (5) to write

$$n \frac{\partial \rho_f}{\partial t} + \rho_f \frac{\partial n}{\partial t} = -\frac{\partial}{\partial y} \left(\frac{\rho_f k}{\eta} \right) \frac{\partial P}{\partial y},$$

where we have also expanded the derivatives on the left hand side. Noting that n and ρ_f both depend on temperature and pressure, we define the associated compressibilities and expansivities as $\beta_n \equiv (1/n)\partial n/\partial P$, $\beta_f \equiv (1/\rho_f)\partial \rho_f/\partial P$, $\lambda_n \equiv (1/n) \partial n/\partial T$ and $\lambda_f \equiv -(1/\rho_f) \partial \rho_f/\partial T$ [see, e.g., Segall and Rice, 1995; Rice, 2006]. Using these definitions, we can write $\partial n/\partial t = n\beta_n(\partial P/\partial t) + n\lambda_n(\partial T/\partial t)$, and a similar expression arises for $\partial \rho_f/\partial t$. Here, we assume that any inelastic dilatant effects take place during a short transient interval at the onset of slip and contribute to setting the initial state from which the system evolves. Substituting into the equation above and defining the expansion ratio $\Lambda \equiv (\lambda_f - \lambda_n)/(\beta_f + \beta_n)$ and storage capacity $\beta \equiv n(\beta_f + \beta_n)$, we find that for $-h/2 \leq y \leq h/2$, the evolution of pore pressure is described by

$$\dot{P} - \Lambda \dot{T} = \alpha_{hy} \frac{\partial^2 P}{\partial y^2}, \quad (6)$$

where the hydraulic diffusivity $\alpha_{hy} \equiv k/(\eta\beta)$ determines the rate at which fluid diffuses from the shear zone.

[11] The storage capacity β provides a measure for how changes in state alter the mass of fluid that can be stored within the porous gouge. Implicit in equation (6) is the assumption that gradients in the hydraulic diffusivity and fluid density are small in comparison to lateral variations in the pressure gradient. Later we will generalize the analysis to examine how the predicted behavior changes when gradients in the properties of the gouge and fluid are accounted for. The physical meaning of the expansion ratio Λ is illuminated by considering the case in which there is no drainage, for example when the permeability is extremely low. In such circumstances, the right side of equation (6) is zero and a temperature change ΔT produces a change in pore pressure of $\Delta P = \Lambda \Delta T$.

[12] Outside the shear zone, for $|y| \geq h/2$, we write

$$\dot{P} - \Lambda \dot{T} = \alpha'_{hy} \frac{\partial^2 P}{\partial y^2}, \quad (7)$$

where the average hydraulic diffusivity is α'_{hy} .

[13] To close the problem, the boundary conditions and initial conditions are as follows. Throughout the model domain the initial temperature is assumed constant and the initial pressure distribution hydrostatic so that $T(y, 0) = T_{amb}$ and $P(y, 0) = P_0$. In the far field, where heat and mass transport are negligible, the boundary conditions are $T(\infty, t) = T_{amb}$ and $P(\infty, t) = P_0$. When dilatancy associated with the passing rupture front [e.g., *Poliakov et al.*, 2002] acts to decrease the pore pressure from the prior ambient value, nonuniform initial and far-field pressure conditions may be encountered. However, with no firm constraints on such processes at present, we leave such complications to future work. Symmetry considerations indicate that there is no heat or mass flow across the midplane so that along $y = 0$ we have $\partial T/\partial y = 0 = \partial P/\partial y$. The temperature and fluid pressure must be continuous across the shear zone boundaries at $y = \pm h/2$. In addition, the conservation of energy and mass, with the assumed conditions of identical ρc and β both within and outside the shear zone, require $(\rho c \alpha_{th}) \partial T/\partial y$ and $(\beta \alpha_{hy}) \partial P/\partial y$ continuous across the shear zone boundaries.

[14] (Before continuing, we note the following: It has been suggested that only a fraction of the work done in shear failure actually shows up as heat, the rest being converted into surface energy of newly formed gouge fragments, or reformed fragments when partly bonded grains separate. To interpret the calculations that follow in circumstances where only a fraction $\psi \leq 1$ of the internal energy change is accountable as temperature rise, we could write the total strength of the fault as $\tau = f_{tot}(\sigma_n - P)$, and define $f = \psi f_{tot}$ so that equation (3) remains the correct expression to calculate the temperature rise. However, the evolution of stress as a function of slip that we calculate is actually $\tau_{heating} = \tau \psi$ vs. slip, and the actual stress, and hence also the fracture energy, would be larger than what we calculate by the fraction $1/\psi$. In the following discussion we assume that $\psi \approx 1$, but emphasize that the calculations are equally valid when ψ is significantly smaller, as long as τ and the fracture energy are rescaled appropriately, and the reported f is viewed to represent the scaled frictional coefficient as well. Should a value of ψ

other than unity be preferred, we leave it to the reader to interpret our results accordingly.)

2.2. Representative Parameters

[15] Many of the results that follow are presented in dimensionless form so that the model predictions can easily be assessed for different choices of parameter values. We note that some of these parameters are less well constrained than others, and indeed part of the motivation in conducting this modeling exercise is to provide understanding as to how different parameter regimes are associated with different limiting behavior during earthquake slip. For example, the appearance or absence of pseudotachylytes (the quenched glasses that are formed from frictionally generated melts) along a given fault system places limits on the ultimate temperature rise during seismic slip; the model predictions can be employed to determine what combinations of physical parameters enable such temperatures to be achieved. We also note that some of the model parameters, such as the permeability to fluid flow, are likely to undergo considerable natural variability from fault to fault and even along different sections of the same fault. Our approach here is not designed to capture the range of this variability, but rather to assign values that derive from specific measurements of fault zone properties that are obtained from the published literature. Insight into the behavior expected from other model scenarios can be obtained by first making the appropriate conversions to dimensionless form and viewing the predictions that follow accordingly.

[16] In Table 1 we summarize the parameter choices that are used to estimate the key scales that characterize the model results. Column 2 represents the nominal values, which are calculated for the ambient pressure and temperature conditions at an assumed centroidal depth of 7 km, with initially hydrostatic pressure at 70 MPa, and a geothermal gradient of 30°C/km. Recognizing that many of the properties of the system are sensitive to changes in pressure and temperature of the magnitude expected during a slip event, columns 3 and 4 are used to illustrate the extent of these changes. Column 3 contains the average parameter values along an assumed pressure and temperature path that is constructed to approximate how the temperature and pressure vary between the fault plane and the ambient, undisturbed gouge beyond the thermal and hydrological boundary layers. For simplicity here, we follow the same procedure as used for Table 2 of *Rice* [2006]. We assume a linear relationship between pore pressure and temperature and average over half the pore pressure rise between hydrostatic and lithostatic, while the temperature increases from ambient to half its maximum value. Column 4 gives the minimum and maximum effective parameter values along the pressure and temperature path that was used for column 3.

[17] To give a specific illustration, the permeability begins at an ambient value of $k = 0.65 \times 10^{-20} \text{ m}^2$. As the pore pressure increases, the permeability increases so that after a finite amount of slip, k is higher on the fault plane than it is at the still reference conditions beyond the thermal and hydrologic boundary layers. We use the average pressure $[P(0, t) + P_0]/2$ and temperature $[T(0, t) + T_{amb}]/2$ to calculate an approximation for the overall permeability in this new state. The effective permeability so obtained rises to $k = 3.38 \times$

Table 1. Representative Parameter Values^a

Parameter	Nominal Value	Average on Elastic $P - T$ Path	Range on Nominal Path	Damaged Value	Average on Damaged $P - T$ Path	Range on Damaged Path
h , mm	0.145	0.145	—	0.145	0.145	—
ρc , MPa/°C	2.7	2.7	—	2.7	2.7	—
V , m/s	1.0	1.0	—	1.0	1.0	—
T_{amb} , °C	210	210	—	210	210	—
$\sigma_n - P_0$, MPa	126	126	—	126	126	—
f	0.25	0.25	—	0.25	0.25	—
n	0.036	0.043	0.036–0.052	0.036	0.043	0.036–0.052
α_{th} , mm ² /s	0.70	0.66	0.61–0.70	0.70	0.54	0.43–0.70
λ_f , 10^{-3} /°C	1.12	1.21	1.12–1.42	1.12	2.30	1.12–3.10
λ_n , 10^{-3} /°C	−0.22	−0.20	(−0.22)–(−0.17)	0.024	0.024	—
β_f , 10^{-9} /Pa	0.70	0.82	0.70–1.00	0.70	5.01	0.70–7.54
β_n , 10^{-9} /Pa	0.74	0.88	0.74–1.04	2.82	3.35	2.82–3.98
η_f , 10^{-4} Pa s	1.47	1.23	1.05–1.47	1.47	0.75	0.55–1.47
k , 10^{-20} m ²	0.65	1.56	0.55–3.38	6.5	15.7	5.5–33.8
β , 10^{-10} /Pa	0.52	0.55	0.52–1.06	1.26	2.97	1.26–5.78
Λ , MPa/°C	0.93	0.89	0.78–0.93	0.31	0.30	0.13–0.40
α_{hy} , mm ² /s	0.86	2.05	0.73–3.05	3.52	6.71	2.99–10.3
L^* , mm	1.69	2.94	1.55–4.87	35.4	57.7	24.5–415
δ_c , mm	1.69	1.82	1.69–2.00	4.24	4.86	3.93–12.1
T_{max}	500	620	—	1520	2240	—

^aAs in Table 2 of Rice [2006]. Fluid properties are taken from Burnham *et al.* [1969], Keenan *et al.* [1978], and Tödheide [1972], gouge properties are from Lachenbruch [1980], Vosteen and Schellschmidt [2003], Wibberley [2002, also private communication 2003], and Wibberley and Shimamoto [2003].

10^{-20} m² when the pore pressure on the fault plane is lithostatic. The temperature on the fault plane at this point is at its highest and we approximate its value here using the ultimate temperature rise predicted using the nominal property values, $T_{\text{max}} \approx 500^\circ\text{C}$. The range of effective permeabilities calculated in this manner is listed in column 4. Clearly, no single value of permeability is representative of conditions throughout the changes in state; however, to gain more intuition for what changes in state are likely to occur, we take the average of the effective permeabilities over the range of average pressures and temperatures encountered, and enter it, $k = 1.56 \times 10^{-20}$ m², in column 3.

[18] Columns 2–4 represent our best estimates for the physical properties assuming that the fault walls deform elastically during rupture. Columns 5–7 represent a scenario in which the fault zone is severely damaged by the passage of the rupture front. As in Table 2 of Rice [2006], we arbitrarily assign an order of magnitude increase to the laboratory-constrained permeability, and we double the drained compressibility used to calculate β_n , as described in the appendix of Rice [2006]. We assume the pore thermal expansivity is equal to the thermal expansivity of the solid grains themselves for this case. Column 7 again represents the range of effective values along the assumed average pressure-temperature path. Note that the parameters given in the upper third of the table are treated as constants throughout the simulations that follow so that no range of values is given in columns 4 and 7. The parameters summarized in the bottom third of the table are calculated from those entered above.

[19] As noted earlier, detailed observations of exhumed faults reveal that the central shear zone during seismic slip is typically of millimeter or submillimeter scale. There is some evidence for temporal variations in the shear zone thickness during a single slip event, but for the current model we take a constant nominal value of h . For each of the simplified, limiting cases described in section 3 a different length scale emerges that characterizes the system evolution; the thickness

$h = 0.145$ mm was chosen to make these length scales equal (e.g., $L^* = \delta_c$) for the nominal parameter values so that the model predictions can be more directly compared. This thickness is within the range reported by Chester and Goldsby [2003] for the localized shear zone within a broader millimeter-scale layer along the Punchbowl fault. We shall see that the ultimate temperature rise predicted for sufficiently long slip is actually independent of h , though the amount of slip required to approach this temperature rise does increase with h . Later, we explore how the predictions from the more comprehensive model change over a range of shear thickness values. Consistent with the degree of approximation used throughout this work, we assume a constant slip rate of $V = 1$ m/s, based on the average results from slip inversions on seven crustal earthquakes by Heaton [1990].

[20] We adopt a nominal friction coefficient of $f = 0.25$. This is much lower than the 0.6–0.8 range characteristic of low-velocity sliding and described by Byerlee’s law. As argued by Rice [2006] and consistent with recent rock physics experiments, the effective friction coefficient during rapid slip at seismogenic depths is expected to be reduced considerably by the effects of flash weakening. This is accounted for in the current models by adopting a constant, lower value for f .

[21] For the nominal parameter values, the storage capacity is $\beta \approx 5.2 \times 10^{-11}$ Pa^{−1}, the expansion ratio is $\Lambda \approx 0.93$ MPa/°C, and the hydraulic diffusivity is $\alpha_{\text{hy}} \approx 0.86$ mm²/s. Of these derived quantities, the range quoted in column 4 makes it clear that the hydraulic diffusivity is the most sensitive to changes in state as the system evolves.

[22] We shall see in section 3 how the system parameters can be grouped to form the length scales L^* and δ_c , which are diagnostic of the overall behavior.

3. Limiting Behavior

[23] Before solving the full set of model equations, we can build considerable insight by examining the limiting

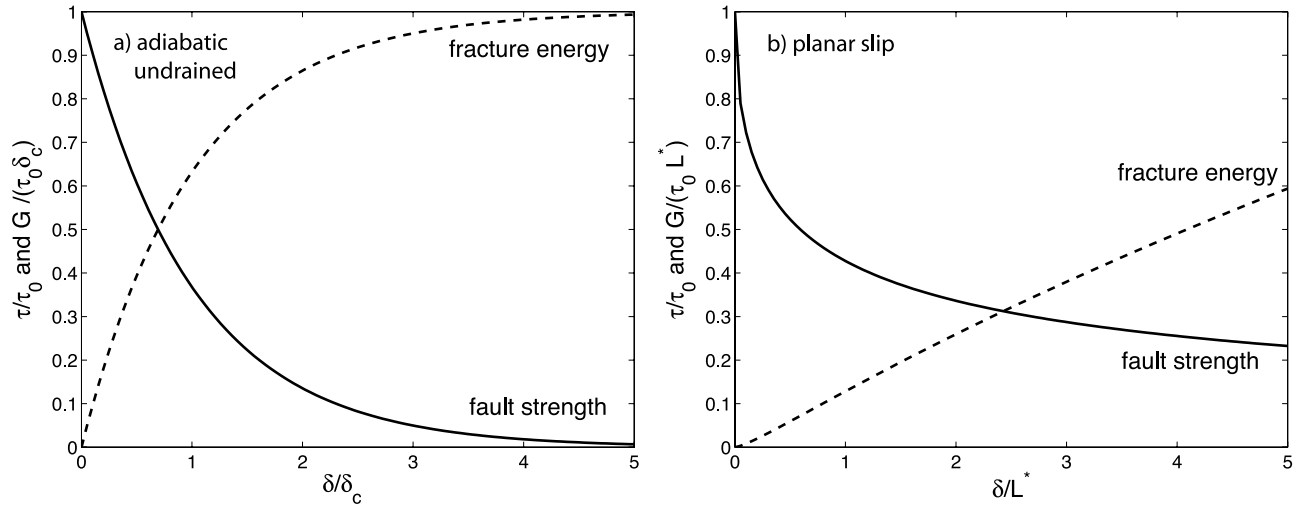


Figure 2. Dimensionless fault strength (solid) and fracture energy (dashed) as a function of scaled slip distance δ . The fault strength decreases with slip from its initial value $\tau_0 = f(\sigma_n - P_0)$. The fracture energy experiences a corresponding increase. (a) Undrained, adiabatic limit, valid for short slip distances. The slip distance δ is scaled by $\delta_c \equiv \rho Ch/(\Lambda f)$. The fracture energy G is scaled by $\tau_0 \delta_c$. (b) Planar slip model, valid for long slip distances. The slip distance δ is scaled by $L^* \equiv (2\rho C/f\Lambda)^2 (\sqrt{\alpha'_{th}} + \sqrt{\alpha'_{hy}})^2/V$. The fracture energy G is scaled by $\tau_0 L^*$. The nominal parameter values were chosen so that $L^* = \delta_c \approx 1.69$ mm, and the scales on these graphs are identical for this case.

behavior of the system under simplified conditions. In particular, for short slip distances the effects of heat and mass transport can be neglected, while for large slip distances, the finite shear zone thickness is expected to have a negligible effect on the system evolution. We briefly describe each of these special cases in turn, using the parameter values summarized in Table 1.

3.1. Short Slip Distances: Negligible Transport

[24] Over short slip distances, the temperature and pore pressure within the fault zone are nearly spatially uniform and the transport of heat and fluid can be neglected. The solutions to equations (3) and (6) for the evolution of temperature and pore pressure in this adiabatic, undrained limit can be written as [Lachenbruch, 1980]

$$\begin{aligned} T(\delta) &= T_{\text{amb}} + \frac{\sigma_n - P_0}{\Lambda} \left[1 - \exp\left(-\frac{\delta}{\delta_c}\right) \right] \\ P(\delta) &= \sigma_n - (\sigma_n - P_0) \exp\left(-\frac{\delta}{\delta_c}\right), \end{aligned} \quad (8)$$

where the thermal-weakening distance $\delta_c \equiv \rho ch/(\Lambda f)$ and the slip distance is $\delta = Vt$.

[25] The maximum predicted temperature rise at long slip distances is not sensitive to the width of the shear zone for this model. It equals $(\sigma_n - P_0)/\Lambda \approx 136^\circ\text{C}$, for the nominal parameter values given in column 2 of Table 1. Using the parameters listed in columns 3, 5, and 6 would lead to corresponding temperature increases of 142°C , 406°C , and 420°C , respectively. Substituting for the pore pressure in equation (1), the predicted fault strength decays exponentially so that $\tau = \tau_0 \exp(-\delta/\delta_c)$, where $\tau_0 = f(\sigma_n - P_0)$ is the initial strength. When there is no fluid transport, the pore pressure rises to balance the normal stress and the fault

strength goes to zero. The fracture energy is defined as a function of slip distance as

$$G(\delta) = \int_0^\delta [\tau(\hat{\delta}) - \tau(\delta)] d\hat{\delta}. \quad (9)$$

For the present case, since no transport is allowed, all the energy released during earthquake slip is transformed into sensible heat. The fracture energy defined by equation (9) is $G = \tau_0 \delta_c = \rho ch (T - T_{\text{amb}}) - \tau \delta$, which scales with the shear zone thickness and becomes equivalent to the total energy released when the final strength tends to zero. The maximum fracture energy at long slip distances is approximately 53 kJ/m^2 for the nominal parameter values. The parameters in columns 3, 5, and 6 in Table 1 lead to predicted maximum fracture energies of 57, 134, and 153 kJ/m^2 , respectively. Figure 2a shows the predicted strength and fracture energy as a function of slip distance for this adiabatic, undrained limit. Using the nominal parameter values from Table 1, the thermal-weakening distance is $\delta_c \approx 1.69$ mm.

3.2. Long Slip Distances: Negligible Thickness

[26] As a second end-member, we examine the case where the shear zone has infinitesimal thickness. The shear acts as a line heat source so that the boundary condition on the temperature gradient at the mid plane becomes

$$\left. \frac{\partial T}{\partial y} \right|_{|y|=0^+} = \mp f[\sigma_n - P(0, t)] \frac{V}{2\rho c \alpha'_{th}}, \quad (10)$$

where $\partial T/\partial y$ is negative for $y > 0$ and positive for $y < 0$. The temperature and pore pressure evolve according to equations (4) and (7), and the remaining boundary conditions are unchanged from before. Defining $L^* =$

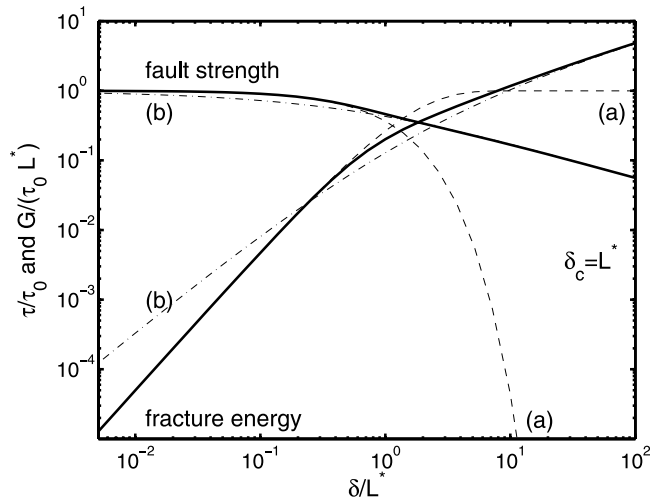


Figure 3. Dimensionless fault strength (decreasing) and fracture energy (increasing) as a function of scaled slip distance δ/L^* . Note the logarithmic scales. The fault strength decreases with slip from its initial value $\tau_0 = f(\sigma_n - P_0)$. The fracture energy experiences a corresponding increase. For comparison, the calculations for the undrained, adiabatic limit are shown with faint dashed lines, labeled (a) on the right. The calculations for the planar slip model are shown with faint dot-dashed lines, labeled (b) on the left. The fracture energy G is scaled by $\tau_0 L^*$. The nominal parameter values from column 2 of Table 1 were used to place all predictions on a common scale with $L^* = \delta_c \approx 1.69$ mm. See the text for further discussion.

$(2\rho c/f\Lambda\sqrt{V})^2(\sqrt{\alpha'_{hy}} + \sqrt{\alpha'_{th}})^2$, we can write the temperature and pressure on the midplane as [Rice, 2006]

$$T(\delta) = T_{\text{amb}} + \left(\sqrt{\alpha'_{hy}} + \sqrt{\alpha'_{th}}\right) \frac{\sigma_n - P_0}{\Lambda\sqrt{\alpha'_{th}}} \left(1 - \exp\frac{\delta}{L^*} \operatorname{erfc}\sqrt{\frac{\delta}{L^*}}\right),$$

$$P(\delta) = P_0 + (\sigma_n - P_0) \left(1 - \exp\frac{\delta}{L^*} \operatorname{erfc}\sqrt{\frac{\delta}{L^*}}\right). \quad (11)$$

With prolonged slip the pore pressure tends toward the normal stress for $\delta \gg L^*$ and the temperature rise approaches the asymptotic limit $\Delta T = (1 + \sqrt{\alpha'_{hy}/\alpha'_{th}})(\sigma_n - P_0)/\Lambda$.

[27] Comparing with the adiabatic, undrained predictions from equation (8) we see that the transport of heat and fluid from the shear zone causes the ultimate temperature rise to increase by a factor of $1 + \sqrt{\alpha'_{hy}/\alpha'_{th}}$. This becomes particularly significant when the hydraulic diffusivity exceeds the thermal diffusivity. For the nominal parameter values in Table 1, $\alpha_{hy} \approx 1.2 \alpha_{th}$ and the final temperature rise is predicted to be approximately 290°C, a factor of 2.1 greater than for the adiabatic, undrained calculation. The predicted temperature rises for columns 3, 5, and 6 of Table 1 are changed even more significantly to 410°C, 1310°C, and 2030°C, respectively.

[28] The fault strength for this case satisfies $\tau = \tau_0 \exp(\delta/L^*) \operatorname{erfc}\sqrt{\delta/L^*}$. Using equation (9), the fracture energy is [Rice, 2006]

$$G(\delta) = \tau_0 L^* \left[\exp\frac{\delta}{L^*} \operatorname{erfc}\sqrt{\frac{\delta}{L^*}} \left(1 - \frac{\delta}{L^*}\right) - 1 + 2\sqrt{\frac{\delta}{\pi L^*}} \right], \quad (12)$$

which can be written for large δ as

$$G \approx \tau_0 L^* \left[\sqrt{\delta/(\pi L^*)} - 1 + 3/2\sqrt{L^*/(\pi\delta)} + \dots \right]. \quad (13)$$

The diffusion of heat and fluid from the shear zone causes the fracture energy to increase with the square root of slip distance for large events. At smaller slip distances, equation (12) is consistent with the seismic estimates of fracture energy made by *Abercrombie and Rice* [2005], who found that $G \propto \delta^{1.3}$ over several decades of slip less than a few decimeters.

[29] The evolution of fault strength and fracture energy for this planar slip model are shown in Figure 2b. The leakage of fluid and heat from the shear zone result in a much more gradual evolution of fault strength and fracture energy at long slip distances than that predicted from the adiabatic, undrained treatment shown in Figure 2a. The nominal parameters in Table 1 yield a characteristic weakening distance $L^* \approx 1.69$ mm. The fracture energy increases monotonically with slip, and has a characteristic scale of $\tau_0 L^* \approx 53$ kJ/m² for the nominal parameter values. For columns 3, 5, and 6, the corresponding energy scales are 93, 1120, and 1820 kJ/m², respectively.

[30] The length scale L^* will be used to plot the dimensionless slip distance in several of the graphs that follow. To display the predictions of the adiabatic, undrained model on the same axes for comparison, even in cases where $L^* \neq \delta_c$, we make use of the relation $\sqrt{L^*V} \equiv 2\delta_c(\sqrt{\alpha_{th}} + \sqrt{\alpha_{hy}})/h$.

4. Distributed Shear

[31] Next we show how the results from section 3 emerge naturally as limiting cases for the predicted state evolution within a finite shear zone when the effects of heat and mass transport are taken into account. We use the numerical procedure outlined in Appendix A to solve the model equations of section 2 for uniform shear in a zone of thickness h .

[32] Logarithmic plots of the predicted fault strength and fracture energy are shown as a function of slip distance in Figure 3. The heavy solid lines give the results in dimensionless form. Using the nominal parameter values from Table 1, the results from the two simplified models in Figure 2 are displayed for comparison. As anticipated, the predicted fault strength and fracture energy are closely approximated by the adiabatic, undrained predictions at small slip distances, whereas at large slip distances the predictions of the planar slip model closely resemble the numerical results. The transition in behavior between these two limiting cases occurs at a slip distance near $\delta = L^* \approx 1.69$ mm for the nominal parameter values. Closer examination reveals that the predicted fault strength experiences a relatively abrupt transition in behavior between the two limits. Because of its integrated dependence on strength history, a somewhat longer range of slip distances characterizes the change in fracture energy from being closely approximated by the adiabatic, undrained model to being well represented by the planar slip model. Nevertheless, for slip distances greater than $\delta \approx 25L^* \approx 0.04$ m, the predictions for both the fracture energy and the fault strength are virtually indistinguishable from those obtained by the planar slip model. In

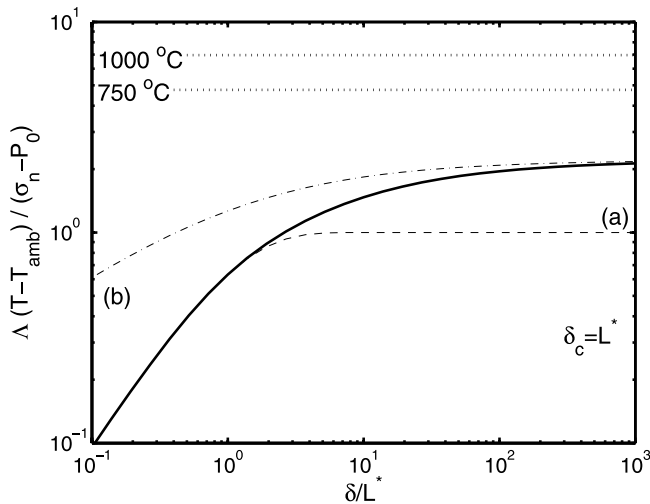


Figure 4. Dimensionless temperature change $\Delta(T - T_{\text{amb}})/(\sigma_n - P_0)$ as a function of scaled slip distance δ/L^* . Note the logarithmic scales, with the x axis shifted one decade from that used in Figure 3. For comparison, the calculations for the undrained, adiabatic limit are shown with a faint dashed line, labeled (a) on the right. The calculations for the planar slip model are shown with a faint dot-dashed line, labeled (b) on the left. For the nominal parameter values from Table 1, the temperature scale $(\sigma_n - P_0)/\Lambda \approx 136^\circ\text{C}$. Assuming that melting begins at 750°C and the initial temperature is 210°C , melting would be expected to begin at a dimensionless temperature of 3.97, as labeled with the horizontal dotted line. A 1000°C melting temperature would correspond to a dimensionless temperature of 5.81. Melting conditions are not achieved for these parameter values.

the case shown here, $\delta_c = L^*$. Further calculations that are discussed below demonstrate that the slip distance characterizing the transition in fault zone behavior depends on both δ_c and L^* . For the purposes of calculating the fault strength and fracture energy at slip distances much greater than both δ_c and L^* , it suffices to use the asymptotic approximation for G from equation (13), while for strength we have [Rice, 2006]

$$\tau \approx \tau_0 \left[\sqrt{\frac{L^*}{\pi\delta}} - \frac{1}{2\sqrt{\pi}} \left(\frac{L^*}{\delta}\right)^{3/2} + \dots \right]. \quad (14)$$

At large slip distances, the diffusion of heat and fluid mass from the shear zone causes the fracture energy to increase with the square root of δ , while the strength decreases with $1/\sqrt{\delta}$.

[33] Figure 4 shows the predicted change in temperature as a function of slip distance. Recall that for the nominal parameter values the characteristic temperature scale is $(\sigma_n - P_0)/\Lambda \approx 136^\circ\text{C}$ and the initial temperature is 210°C . Once again, the adiabatic, undrained predictions closely approximate the numerical results at short slip distances, and the planar slip model gives a better fit at long slip distances. However, neither simplified model does a particularly good job of representing the results over the broad intermediate range of $L^* \leq \delta \leq 10^3 L^*$, that is, from 1.69 mm to 1.69 m, a distance

that characterizes the total slip for many seismic events. This highlights the need to consider both the transport of heat and mass, and the finite shear zone thickness in order to obtain accurate predictions for the temperature rise.

[34] To further illustrate the effects of the finite shear zone thickness, in Figure 5 we show the model predictions when h is increased by a factor of 5 to 0.725 mm , so that $\delta_c = 5L^*$. All other parameters are kept at the nominal values listed in Table 1. The behavior is still well represented by the adiabatic, undrained predictions at short slip distances and by the planar slip model at long slip distances. However, with the increased shear zone thickness the transition between the two sets of limiting behavior occurs at a much larger slip distance. This is to be expected, as the adiabatic, undrained predictions give a good approximation for the more complete model behavior until $\delta > \delta_c$.

[35] A comparison of the fault strength and fracture energy predicted for three different shear zone thicknesses, separated from each other by factors of 5, is shown in Figure 6. In each case, the predicted behavior exhibits a transition between the limiting predictions of the adiabatic, undrained (not shown) and the planar slip models. It is interesting to note, however, that for some ranges of slip distance the model behavior does not experience a monotonic progression as a function of h . For example, examining the fracture energy at a slip distance of $\delta \approx L^* \approx 1.69 \text{ mm}$, the value of G for $\delta_c = 5L^*$ ($h = 0.725 \text{ mm}$) is exceeded by the fracture energy for the $\delta_c = 0.2L^*$ ($h = 0.029 \text{ mm}$) case, which is itself exceeded by G calculated for $\delta_c = L^*$ ($h = 0.145 \text{ mm}$). The apparent nonlinearity is a direct consequence of changes in the amount of slip required for the adiabatic, undrained model to lose its validity (e.g., compare the point where the solid and dashed lines first deviate in Figures 3 and 5) as the effects of heat and mass transport

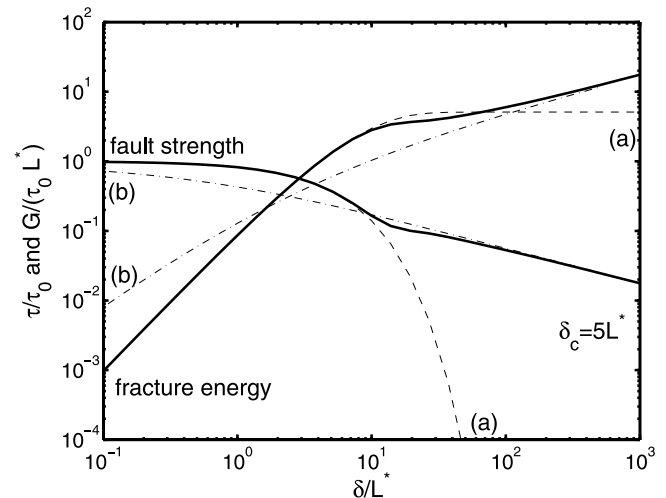


Figure 5. Dimensionless fault strength (decreasing) and fracture energy (increasing) as a function of scaled slip distance δ/L^* , as in Figure 3 but with $\delta_c = 5L^*$. For comparison, the calculations for the undrained, adiabatic limit are shown with faint dashed lines, labeled (a) on the right. The calculations for the planar slip model are shown with faint dot-dashed lines, labeled (b) on the left. The fracture energy G is scaled by $\tau_0 L^*$. The length scale $L^* \approx 1.69 \text{ mm}$, and the length scale $\delta_c \approx 5L^* \approx 8.45 \text{ mm}$.

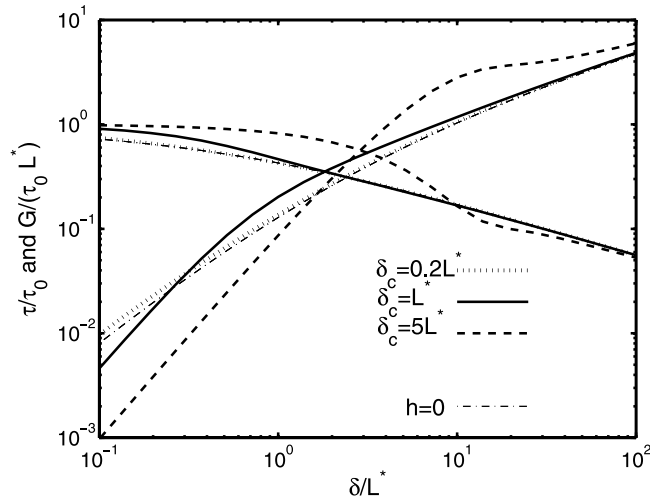


Figure 6. Dimensionless fault strength and fracture energy as a function of scaled slip distance δ/L^* for three different shear zone thicknesses: $h = 0.029$ mm ($\delta_c = 0.2L^*$, dotted), $h = 0.145$ mm ($\delta_c = L^*$, solid) and $h = 0.725$ mm ($\delta_c = 5L^*$, dashed). The calculations for the planar slip model are shown with faint dot-dashed lines, which are largely obscured by the dotted lines for the calculation with $h = 0.029$ mm. The fracture energy G is scaled by $\tau_0 L^*$. The length scale $L^* \approx 1.69$ mm.

gain in importance. A thicker shear zone retains most of its heat and fluid for a longer slip duration before the gradients that drive significant flow are established; at intermediate slip distances the dependences of fracture energy and strength on shear thickness need not be monotonic.

4.1. Comparison With Gaussian Shear

[36] In the present work, we have made no attempt at modeling how the shear is expected to be distributed, but rather have made an a priori assumption for the form of $\dot{\gamma}(y, t)$. The previous calculations have been made for the case where $\dot{\gamma} = V/h$, so that the shear rate is uniform throughout the layer. This particular choice of shear distributions is symmetric about the midplane, and has the virtue of simplicity, but it is also admittedly ad hoc. An alternative assumption, proposed by *Andrews* [2002], is that the shear rate takes a Gaussian distribution of the form

$$\dot{\gamma} = \frac{V(t)}{\sqrt{2\pi}w} \exp\left(\frac{-y^2}{2w^2}\right), \quad (15)$$

where w measures the effective thickness of the shearing zone and $V(t)$ is the net slip rate, as before. This formulation allows for more rapid shear closer to the midplane where the pore pressure is most significantly elevated. In Figure 7 we compare the predictions generated by the Gaussian shear distribution with those of the uniform shear case discussed earlier. (Details of the calculations are presented in Appendices A and B.) At large slip distances, the predicted behavior of the two models coincides. As we have already demonstrated for the case of uniform shear, when the width of the thermal and hydrological boundary layers greatly exceeds the shear zone thickness, corresponding to condi-

tions where $\delta \gg L^*$ and $\delta \gg \delta_c$, the behavior is well approximated by the simplified model for slip on a plane. As could be anticipated, here we see that the same is true when the shear has a Gaussian distribution, and indeed we expect this to be a general feature of all shear distributions that are symmetric about the midplane. At low slip distances, the behavior is more sensitive to the precise distribution of shear. Some of these differences are related to the particular choices for w and h . For the solid lines we have taken $w = h$, but in fact this means that along the midplane the shear rate predicted for the Gaussian distribution is a factor of $\sqrt{2\pi}$ slower than that for the case of uniform shear. The dotted line shows that for short slip distances, the predictions of the uniform shear model are more closely aligned with the Gaussian model predictions when the effective width is reduced by a factor of $\sqrt{2\pi}$.

4.2. Conditions for Melt Onset

[37] It has been suggested that the geologic evidence for melting in mature fault zones (e.g., faults that are marked by thick gouge layers and that have accommodated many large earthquakes) is relatively rare [e.g., *Sibson and Toy*, 2006]. It is still debated whether the preservation of melt products, principally pseudotachylytes, might explain the scarcity of such observations or whether they may actually be taken to imply a rarity of melting conditions. We note in passing that impressive deposits of melt products have indeed been found [e.g., *Rowe et al.*, 2005]. In either case, it is instructive to consider what conditions are required to achieve melting conditions. If the absence of evidence for such conditions along exhumed fault segments can be interpreted as evidence for the absence of such heating events, then the model predictions can be inferred to set

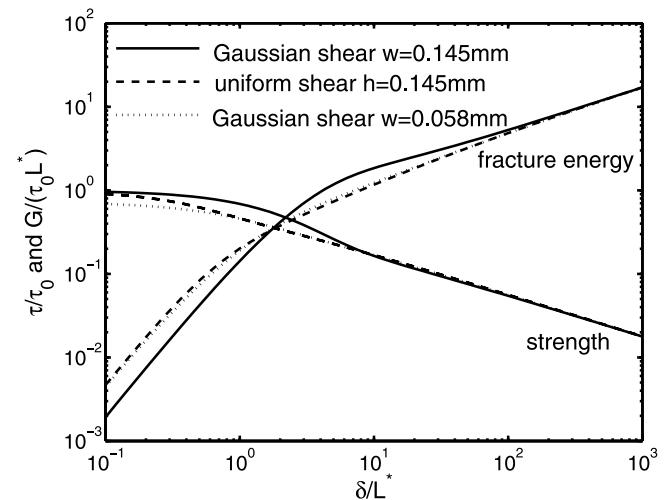


Figure 7. Dimensionless fault strength and fracture energy as a function of scaled slip distance δ/L^* for two distributed shear models. The dashed lines show the predicted evolution when the shear is uniform through a layer of thickness $h \approx 0.145$ mm, so that $\delta_c = L^*$. The solid lines show the predicted behavior when the shear has the Gaussian distribution proposed by *Andrews* [2002], with characteristic width $w \approx 0.145$ mm. The dotted lines show the predictions when w is reduced by a factor of $\sqrt{2\pi}$.

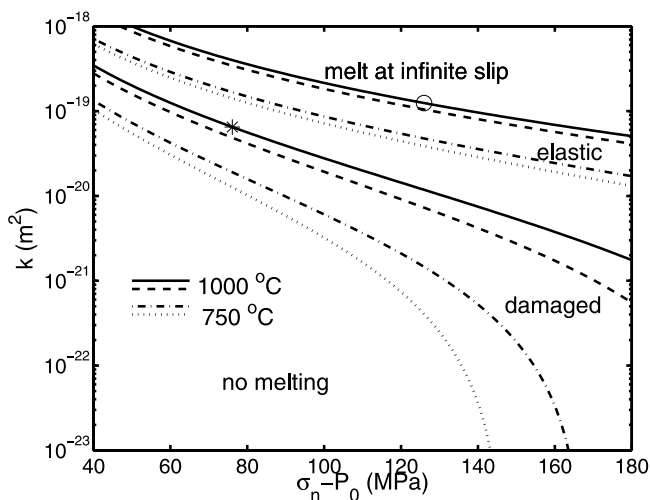


Figure 8. Regime diagram showing the permeability as a function of initial effective stress required for melting conditions to be reached. The upper two pairs of curves were calculated assuming elastic behavior with the parameters summarized in columns 2 (upper) and 3 (lower) in Table 1. The solid and dashed curves are for an assumed melt onset of 1000°C, the dot-dashed and dotted curves are for a melt onset of 750°C. The lower two pairs of curves show the corresponding calculations assuming damaged fault walls and the parameter values summarized in columns 5 and 6 of Table 1. For each case, the initial temperature was taken as $T_{amb} = 210^\circ\text{C}$. Calculations are valid in the limit of long slip for distributed shear. We note that for the lowermost dotted curve, calculated using the parameters from column 6 of Table 1, the undrained adiabatic model indicates that a temperature of 750°C is reached at $\sigma_n - P_0 \approx 147$ MPa; at higher effective stresses and with long enough slip, this melt onset temperature is reached no matter how low the permeability. Similarly, for the lowermost dot-dashed curve, calculated using the column 5 parameters, the undrained adiabatic model predicts that a temperature of 750°C is reached with long enough slip when $\sigma_n - P_0 \approx 168$ MPa.

bounds on the allowable range of some of the less well constrained physical parameters in the system.

[38] The dotted lines in Figure 4 show temperatures of 750°C and 1000°C, which are values typical of the onset of melting. Melting does not occur when the nominal parameter values are used. By contrast, for example, the highly damaged fault zone represented by the parameters in column 5 of Table 1 would be expected to begin melting with large enough slip, ultimately leading to a temperature rise of 1310°C, as noted in section 3. We should emphasize that additional physical interactions become important once melting actually begins and the current model is not formulated to treat the subsequent evolution of the system.

[39] Regime diagrams can be constructed to distinguish between parameter choices for which melting will or will not occur. An example is shown in Figure 8, with the permeability required to achieve melting plotted as a function of the initial effective stress for the different parameter choices summarized in Table 1. The uppermost pair of curves represent a temperature rise of 790°C, from

210°C to 1000°C using the parameter values from columns 2 and 3 of Table 1. The next pair repeat the calculations for a temperature rise of 540°C, from 210°C to 750°C. The corresponding results for the data listed in columns 5 and 6 of Table 1 are shown with the lower two pairs of curves. Calculations were performed using the long-term limit from the planar slip model $\Delta T = (\sigma_n - P_0)/\Lambda(1 + \sqrt{\alpha_{hy}/\alpha_{th}})$, which also corresponds to the asymptotic temperature rise for both distributed shear models. The onset of melting is facilitated by the more efficient fluid escape associated with higher permeabilities and by the larger increase in pore pressure possible with higher initial values of the effective stress. Enhanced pore expansivity also acts to promote the onset of melting, as evidenced by the differences between the damaged and elastic results.

[40] Figure 9 shows how the slip distance δ_m required for the onset of melting varies with the permeability at the fixed nominal value $\sigma_n - P_0 = 126$ MPa for the initial effective stress. The dotted horizontal line corresponds to the point labeled by the circle on the uppermost solid curve in Figure 8, that is, the permeability and effective stress required for melting to begin at 1000°C with an unbounded amount of slip, using the nominal parameter values in column 1 of Table 1. The solid curves in Figure 9 show the slip distance required for melting to begin at 7 km depth at different, labeled values of the shear zone thickness h . Of particular note are the slip deficits between the dashed line that shows the predictions of the $h = 0$ planar slip limit, and the curves

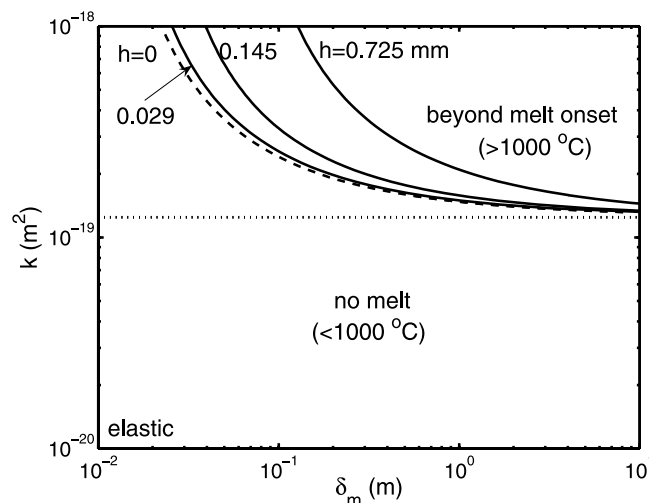


Figure 9. Regime diagram showing the permeability as a function of slip distance required for melting conditions to be reached, for the labeled shear zone thickness h in millimeters, and the nominal parameter values from column 2 of Table 1. The initial temperature was taken as $T_{amb} = 210^\circ\text{C}$, with melting assumed to begin at $T_m = 1000^\circ\text{C}$. The model predicts that melting begins to occur for a given permeability and shear zone thickness when the slip reaches the corresponding solid line. The dashed line shows the calculations for the planar slip model, which underpredicts the slip required for melt onset in a finite shear zone. In the region below the horizontal dotted line, melting will not occur no matter how long the slip.

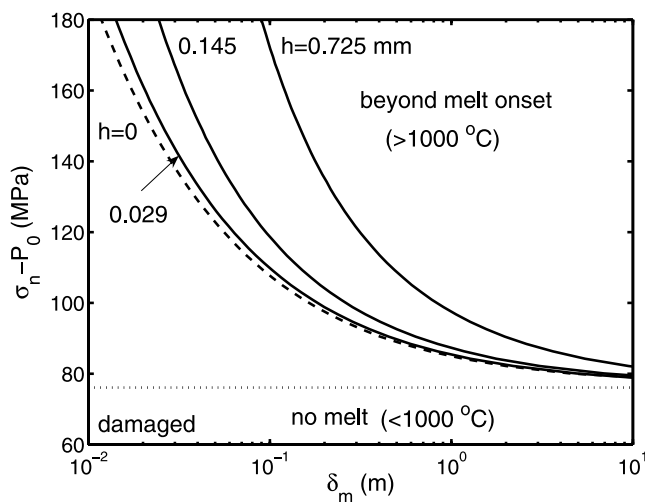


Figure 10. Regime diagram showing the initial effective stress as a function of slip distance required for melting conditions to be reached, for the labeled shear zone thickness h in millimeters, and the damaged parameter values from column 5 of Table 1. The initial temperature was taken as $T_{\text{amb}} = 210^\circ\text{C}$, with melting assumed to begin at $T_m = 1000^\circ\text{C}$. The model predicts that melting begins to occur for a given initial effective stress and shear zone thickness when the slip reaches the corresponding solid line. The dashed line shows the calculations for the planar slip model, which underpredicts the slip required for melt onset in a finite shear zone. In the region below the horizontal dotted line, melting will not occur no matter how long the slip.

that correspond to the predictions of the numerical model for finite shear zone thickness. Even for moderately large slip distances of 1 m or more, there is a significant range of parameter values for which the planar slip model would predict the onset of melting, whereas the more complete, distributed shear model indicates that the temperature has not yet reached the melt threshold. As expected, the difference becomes increasingly prominent for greater shear zone thicknesses.

[41] Figure 10 illustrates how the slip distance δ_m required for the onset of melting varies with the initial effective stress at a fixed value of the permeability $k = 6.5 \times 10^{-19} \text{ m}^2$ that is taken as representative of damaged fault walls. The dotted horizontal line corresponds to the point labeled with the asterisk on the lower solid curve in Figure 8, calculated using the parameter values in column 5 of Table 1. As for Figure 9, the different curves correspond to predictions for the labeled shear zone thicknesses.

[42] The parameters chosen for the preceding calculations were taken as representative of conditions at a depth of 7 km with ambient hydrostatic pore pressure and lithostatic normal stress. To predict how the temperature change is expected to vary with depth, we performed a series of calculations in which the fault zone properties were adjusted to represent the effects of an assumed geothermal gradient of $30^\circ\text{C}/\text{km}$, with ambient hydrostatic (10 MPa/km) and lithostatic (28 MPa/km) gradients for the pore pressure and normal stress. As was the case for the values summarized in

Table 1, the fluid expansivities and compressibilities were determined as a function of pore pressure and temperature from the ninth-order polynomial fit to density data reported by *Burnham et al.* [1969]. The fluid viscosities were obtained from spline fits to the data of *Tödheide* [1972]. The formula for the thermal conductivity reported by *Vosteen and Schellschmidt* [2003] was used to calculate how the thermal diffusivity changes as a function of the ambient temperature, keeping the heat capacity constant throughout, and consistent with the value reported by *Lachenbruch* [1980] used in Table 1. The properties of the gouge were derived from the data of *Wibberley* [2002, private communication 2003], and *Wibberley and Shimamoto* [2003]. In particular, exponential fits to the void fraction n and the difference between the drained and solid compressibilities summarized in Table 1 of *Rice* [2006], were used to calculate β_n and λ_n using the formulation described in the appendix of *Rice* [2006]. For the case of elastic fault walls, we used spline fits to the permeability data shown with filled solid circles in Figure 8ii(b) of *Wibberley and Shimamoto* [2003], which were obtained on loading gouge samples from the central slip zone of the Median Tectonic Line fault over a range of effective stress from 10 to 180 MPa. In calculations performed to represent the effects of fault zone damage, we increased the permeability by an order of magnitude and set λ_n equal to the expansivity of the gouge grains and β_n equal to twice the drained compressibility, as discussed further by *Rice* [2006] and consistent with the values reported in column 5 of Table 1.

[43] Figure 11 shows the predicted temperature on the symmetry plane as a function of depth for the different labeled slip distances. Through most of the range, the predicted temperature increases monotonically with depth.

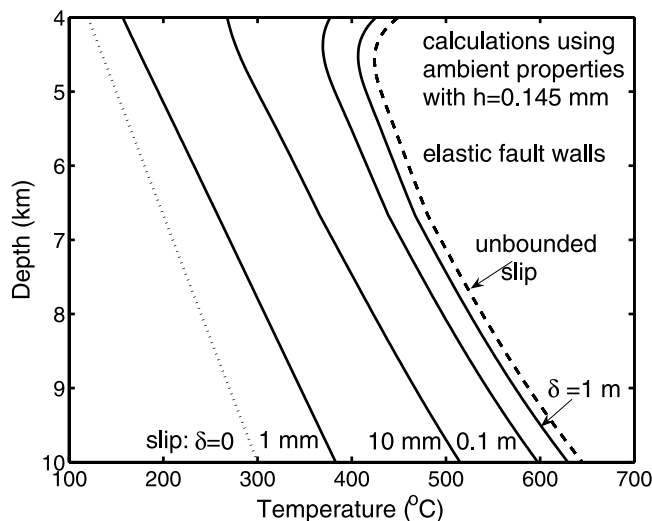


Figure 11. Maximum shear zone temperature as a function of depth for the different labeled amounts of slip, assuming uniform shear with $h = 0.145 \text{ mm}$ and elastic fault walls. The dotted line on the left represents the ambient temperature for a geothermal gradient of $30^\circ\text{C}/\text{km}$. The dashed line on the right shows the asymptotic temperature rise for unbounded slip. Model calculations were performed using parameters derived from the ambient property values, which were interpolated as described in the text.

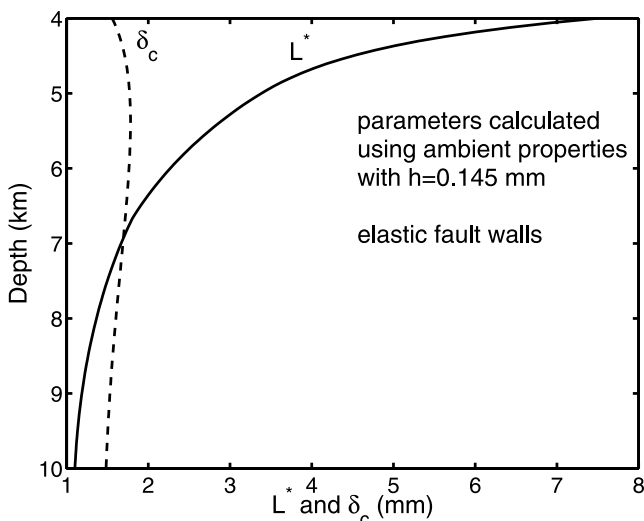


Figure 12. Depth profiles for the length scales L^* and δ_c used in the calculations for Figure 11.

However, with sufficiently large slip at shallow depths there is a slight decrease in the predicted temperature with depth. The source of this behavior is illuminated by examining the profiles of the length scales L^* and δ_c shown in Figure 12. The change in expansion ratio Λ with depth is reflected in the variation of δ_c , which is quite modest over the depth range shown. Recall that the ultimate temperature rise with unbounded slip is proportional to the initial effective stress, which increases linearly with depth, and inversely proportional to the expansion ratio Λ , which as we have seen changes only slightly. However, the temperature rise and L^* are both also sensitive to the ratio of the hydraulic and thermal diffusivities. It is the marked increase in permeability nearer to the ground surface that both causes the rapid increase in L^* toward shallower depths and also overwhelms the effective stress dependence to produce the decrease in predicted temperature with depth with prolonged slip that is shown near the top of Figure 11. For the particular set of parameters chosen, we do not predict the onset of melting over this depth range.

[44] We note that the evolution of strength and fracture energy at any particular location along this depth range can be easily extracted from the information given in Figures 12 and 6. For example at 4 km depth $\delta_c \approx 0.2 L^*$, where $L^* = 7.5$ mm, so the dotted lines in Figure 6 track the predicted behavior, where the initial strength is $\tau_0 \approx 18$ MPa when the effective friction coefficient is 0.25. At 10 km depth, Figure 12 indicates that $\delta_c \approx 1.35 L^*$ and $L^* \approx 1.1$ mm.

[45] Figure 13 again shows the predicted temperature profile following different amounts of slip, but this time treating the case of highly damaged fault walls by increasing the permeability and adjusting the values of β_n and λ_n , as discussed above. As expected, the predicted temperature rise is much greater than that for the case of elastic fault walls shown in Figure 11. Over the entire depth range, melting is expected with slips greater than approximately 0.1 m. At larger slip distances, the effects of the increased permeability nearer the surface become increasingly prominent. The maximum temperature for this selection of parameter values actually occurs nearest the surface for

unbounded slip. This somewhat surprising prediction further highlights the importance of obtaining better constraints on the fluid transport properties and particularly the manner in which they are influenced by damage. We emphasize that while we have made every attempt to faithfully represent the effects of damage in our choice of parameters for these calculations, the factor of ten used to augment the permeability and the choices made for β_n and λ_n are poorly constrained. Given the relative scarcity of evidence for melts generated at shallow seismogenic depths along mature faults, the modeling results presented here suggest that the effects of damage do not normally produce the combination of high permeabilities and altered elastic parameters β_n and λ_n used to obtain the profile shown in Figure 13.

5. Influence of State-Dependent Property Variations

[46] The previous results have all been produced from calculations that used constant values for the properties throughout time. The predicted changes in state are significant, however, and as illustrated in Table 1, are expected to cause correspondingly large changes to the controlling properties. As we have seen, the ratios of parameters that combine to produce the length scales L^* and δ_c determine the predicted behavior when the uniform shear model is evaluated with constant parameter values. However, column 4 of Table 1 indicates that the characteristic scale L^* changes by roughly

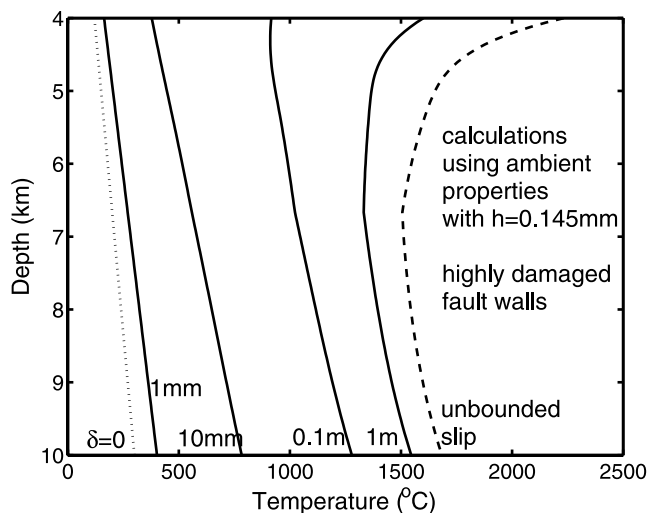


Figure 13. Maximum shear zone temperature as a function of depth for the different labeled amounts of slip, assuming uniform shear with $h = 0.145$ mm and highly damaged fault walls. The dotted line on the left represents the ambient temperature for a geothermal gradient of $30^\circ\text{C}/\text{km}$. The dashed line on the right shows the asymptotic temperature rise for unbounded slip. Damage was simulated by increasing the permeability by an order of magnitude from that used for Figure 11, assuming β_n equals twice the drained compressibility, and assuming that λ_n is equal to the thermal expansivity of the solid gouge grains. As discussed further in the text, at 7 km depth these choices are consistent with those used in column 5 of Table 1. All other properties were the same as those used for Figure 11.

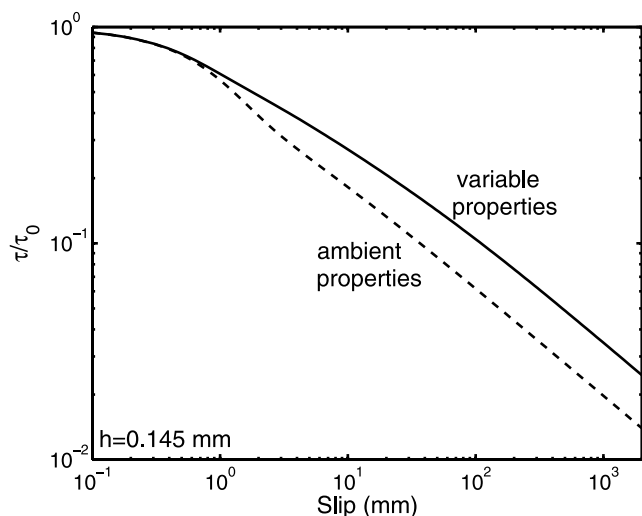


Figure 14. Scaled fault strength as a function of slip distance δ for the uniform shear model. The dashed line shows the results calculated using constant physical properties evaluated under the ambient conditions. The solid line incorporates the effects of variations in properties produced by the changing pressure and temperature state.

a factor of 3 when it is evaluated at the average pressure and temperature near the shear zone for the case where the fault zone behaves elastically; there is an 18% change in the corresponding value of δ_c . When the fault zone is highly damaged, column 7 of Table 1 notes changes in L^* by a factor of 17 and changes in δ_c by a factor of 3. For the case of elastic behavior, the changes in permeability with effective

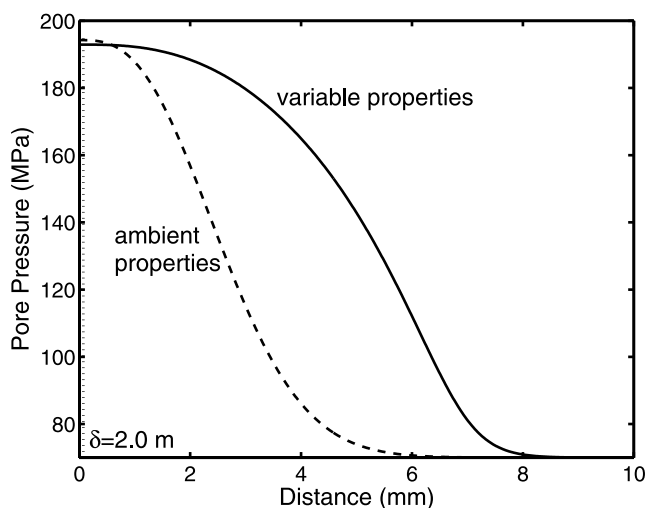


Figure 15. Predicted pore pressure P as a function of distance y normal to the fault midplane for the uniform shear model with $h = 0.145$ mm after a slip distance of $\delta = 2.0$ m. The dashed line shows the results calculated using constant physical properties evaluated under the ambient conditions. The solid line incorporates the effects of variations in properties produced by the changing pressure and temperature state.

stress are by far the most significant variations. Permeability changes are also considerable for the case of the damaged fault zone, but in addition there is a larger predicted temperature range and this produces more significant variations in the fluid properties.

[47] The solution procedure used for the distributed shear models in section 4 is ideal for tracking the predicted behavior over a broad range of slip distances. However, it is not amenable to exploring the nonlinear effects produced by gradients in fault zone properties. Instead, a semidiscretized finite difference code was implemented to examine the sensitivity of the predicted state evolution to property variations. Details of the calculations are provided in Appendix C.

[48] Figure 14 shows a comparison between the fault strength predicted using the constant, nominal parameter values, evaluated in the ambient state, with the predictions for the case where the effects of gradients in the system properties are taken into account. The predictions coincide at slip distance that are short in comparison with L^* , which is initially 1.69 mm for both calculations. At longer slip distances the strength predicted by the variable property model exceeds slightly that predicted for the ambient property calculations. The comparison of predicted pore pressure profiles shown in Figure 15 hints at the cause of this difference. The zone of elevated pore pressures predicted by the variable property calculation is much broader than that predicted by the ambient property calculation. The increase in permeability with pore pressure promotes enhanced fluid transport from the shear zone and a reduction in pore pressure gradients nearest the symmetry plane. The higher fault strength that results produces more rapid shear heating, as shown in Figure 16. After 2 m of slip the predicted temperature rise from the variable property calculation exceeds that of the ambient property

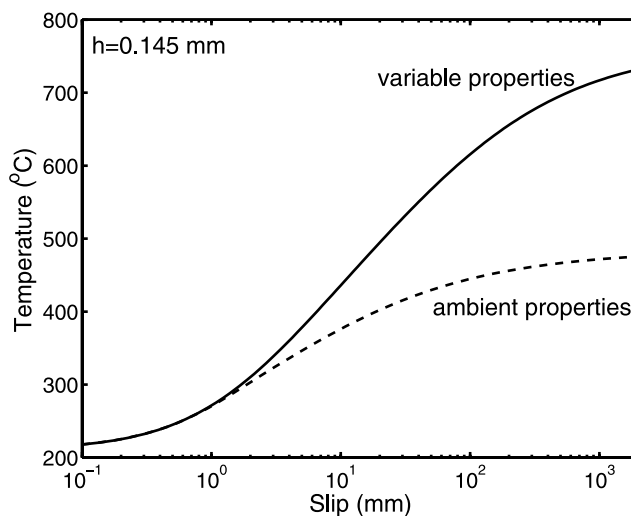


Figure 16. Predicted temperature T as a function of slip distance δ for the uniform shear model. The dashed line shows the results calculated using constant physical properties evaluated under the ambient conditions. The solid line incorporates the effects of variations in properties produced by the changing pressure and temperature state.

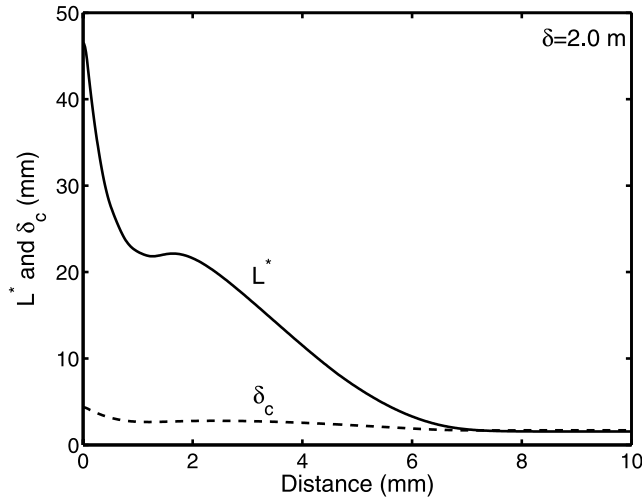


Figure 17. Values of the length scales L^* (solid) and δ_c (dashed) as a function of distance y normal to the fault midplane for the uniform shear model with $h = 0.145$ mm after a slip distance of $\delta = 2.0$ m. Physical properties were adjusted for the local pressure and temperature conditions, as described in the text.

calculation by 50%. The combined influence of temperature and pore pressure on the fluid density and viscosity lead to the complex dependence of L^* on y that is seen in Figure 17. In particular, since the thermal diffusivity is smaller than the hydraulic diffusivity, the temperature remains nearly constant at the ambient level for distances greater than a few millimeters from the symmetry plane. In contrast, the pore pressure does not have appreciable lateral variations in the vicinity of the symmetry plane, but experiences large gradients beyond the thermal boundary layer and so influences the fluid properties at distances where thermal effects are negligible. Since the temperature increase is greater than that predicted from the constant, ambient property calculations, the range in L^* and δ_c is larger than indicated in column 4 of Table 1.

6. Conclusions

[49] By exploring the effects of thermal pressurization during the distributed shear of a thin gouge layer, we have shown that the evolution of strength and fracture energy are represented well by the idealized planar slip model [Rice, 2006] once the slip distance δ is large in comparison to the length scales L^* and δ_c . The thermal evolution is also closely approximated by the predictions of the planar slip model once the slip is sufficiently large. During typical seismic events, however, the accumulated displacement is not extensive enough to reach this limit and the planar slip approximation significantly overestimates the temperature rise. This highlights the critical role of the shear layer thickness in determining the ultimate temperature rise and whether or not melting conditions are achieved. Within the gouge layer, the shear distribution itself does not exert a strong control on the system evolution. However, the behavior of the fault walls, and in particular the potential for damage-enhanced fluid transport and pore compressibility,

are extremely important. Better constraints on these effects are needed for improved quantitative predictions. In the elastic limit, where damage is negligible, melt onset is expected to be relatively rare. Accounting for the influence of lateral gradients in the fluid transport properties does lead to higher predicted temperatures, but still insufficient for melt onset at moderate seismogenic depths (e.g., 7 km for the set of parameters used for Figure 16), even for relatively long slips. When the fault walls are highly damaged, fluid can escape more efficiently from the pressurized shear zone, so the fault strength decreases more slowly and the onset of melting is promoted.

Appendix A: Uniform Shear, $\dot{\gamma} = V/h$

[50] We solve equations (3), (4), (6) and (7) using Laplace transforms, making the usual definitions

$$\begin{aligned}\tilde{f}(s) &= \int_0^\infty \exp(-st)f(t)dt \\ f(t) &= \frac{1}{2\pi i} \int_{\gamma-i\infty}^{\gamma+i\infty} \exp(st)\tilde{f}(s) ds\end{aligned}$$

so that in the transform domain we have

$$\begin{aligned}s\tilde{P} - P_0 - \Lambda(s\tilde{T} - T_{\text{amb}}) &= \alpha_{hy} \frac{d^2\tilde{P}}{dy^2} & |y| < \frac{h}{2} \\ s\tilde{T} - T_{\text{amb}} - V[\sigma_n - \tilde{P}(0, s)] &= \alpha_{th} \frac{d^2\tilde{T}}{dy^2} \\ s\tilde{P} - P_0 - \Lambda(s\tilde{T} - T_{\text{amb}}) &= \alpha'_{hy} \frac{d^2\tilde{P}}{dy^2} & |y| > \frac{h}{2} \\ s\tilde{T} - T_{\text{amb}} &= \alpha'_{th} \frac{d^2\tilde{T}}{dy^2}.\end{aligned}\quad (\text{A1})$$

In addition, the boundary conditions discussed earlier require that the temperature and pressure gradients vanish at $y = 0$, the temperature and pressure remain finite at large y , and the temperature, pressure, heat flux and mass flux stay continuous across the shear zone boundary. For the

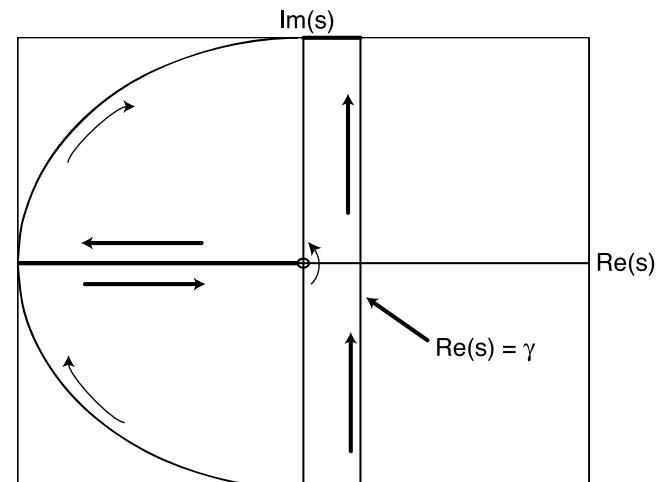


Figure A1. Contour integral for Laplace inversion (see description in text).

special case in which $\alpha_{th} = \alpha'_{th}$ and $\alpha_{hy} = \alpha'_{hy}$, the solutions in the transform domain are

$$\tilde{P} = \frac{P_0}{s} + \Lambda C + \frac{\Lambda C}{\alpha_{hy} - \alpha_{th}} \left[-\alpha_{hy} \exp\left(-\frac{h}{2} \sqrt{\frac{s}{\alpha_{hy}}}\right) \cosh\left(y \sqrt{\frac{s}{\alpha_{hy}}}\right) + \alpha_{th} \exp\left(-\frac{h}{2} \sqrt{\frac{s}{\alpha_{th}}}\right) \cosh\left(y \sqrt{\frac{s}{\alpha_{th}}}\right) \right] \quad |y| < \frac{h}{2}$$

$$\tilde{T} = \frac{T_{amb}}{s} + C - C \exp\left(-\frac{h}{2} \sqrt{\frac{s}{\alpha_{th}}}\right) \cosh\left(y \sqrt{\frac{s}{\alpha_{th}}}\right)$$

$$\tilde{P} = \frac{P_0}{s} + \frac{\Lambda C}{\alpha_{hy} - \alpha_{th}} \left[\alpha_{hy} \exp\left(-|y| \sqrt{\frac{s}{\alpha_{hy}}}\right) \sinh\left(\frac{h}{2} \sqrt{\frac{s}{\alpha_{hy}}}\right) - \alpha_{th} \exp\left(-|y| \sqrt{\frac{s}{\alpha_{th}}}\right) \sinh\left(\frac{h}{2} \sqrt{\frac{s}{\alpha_{th}}}\right) \right] \quad |y| > \frac{h}{2}$$

$$\tilde{T} = \frac{T_{amb}}{s} + C \exp\left(-|y| \sqrt{\frac{s}{\alpha_{th}}}\right) \sinh\left(\frac{h}{2} \sqrt{\frac{s}{\alpha_{th}}}\right)$$

where

$$C = \frac{V[\sigma_n - \tilde{P}(0, s)]}{s} = \frac{V\left(\sigma_n - \frac{P_0}{s}\right)}{s + \Lambda V \left[1 - \frac{\alpha_{hy}}{\alpha_{hy} - \alpha_{th}} \exp\left(-\frac{h}{2} \sqrt{\frac{s}{\alpha_{hy}}}\right) + \frac{\alpha_{th}}{\alpha_{hy} - \alpha_{th}} \exp\left(-\frac{h}{2} \sqrt{\frac{s}{\alpha_{th}}}\right) \right]}.$$

As we are mainly interested in the evolution of conditions on the midplane, we set $y = 0$ and write

$$P(0, t) = \frac{1}{2\pi i} \int_{\gamma-i\infty}^{\gamma+i\infty} \exp(st) \tilde{P}(0, s) ds,$$

$$T(0, t) = \frac{1}{2\pi i} \int_{\gamma-i\infty}^{\gamma+i\infty} \exp(st) \tilde{T}(0, s) ds,$$

where

$$\tilde{P}(0, s) = \sigma_n - \frac{s(\sigma_n - \frac{P_0}{s})}{s + \Lambda V \left[1 - \frac{\alpha_{hy}}{\alpha_{hy} - \alpha_{th}} \exp\left(-\frac{h}{2} \sqrt{\frac{s}{\alpha_{hy}}}\right) + \frac{\alpha_{th}}{\alpha_{hy} - \alpha_{th}} \exp\left(-\frac{h}{2} \sqrt{\frac{s}{\alpha_{th}}}\right) \right]},$$

and

$$\tilde{T}(0, s) = \frac{T_{amb}}{s} + \frac{V\left(\sigma_n - \frac{P_0}{s}\right) \left[1 - \exp\left(-\frac{h}{2} \sqrt{\frac{s}{\alpha_{th}}}\right) \right]}{s + \Lambda V \left[1 - \frac{\alpha_{hy}}{\alpha_{hy} - \alpha_{th}} \exp\left(-\frac{h}{2} \sqrt{\frac{s}{\alpha_{hy}}}\right) + \frac{\alpha_{th}}{\alpha_{hy} - \alpha_{th}} \exp\left(-\frac{h}{2} \sqrt{\frac{s}{\alpha_{th}}}\right) \right]} \quad (A2)$$

We evaluate these integrals numerically and use the results to determine the evolution of strength, fracture energy and temperature.

[51] Figure A1 shows a schematic diagram of the contour integral we must perform. The vertical arrows show the path

along which the Laplace inversion is defined from $s = \gamma - i\infty$ to $\gamma + i\infty$. The functions $\tilde{P}(0, s)$ and $\tilde{T}(0, s)$ are analytic in the negative real half plane, except along the branch cut that traces the negative real axis, and possibly at one or more pairs of off-axis poles (not shown). To evaluate equation (A2) for $P(0, t)$ and $T(0, t)$, we choose a contour that starts at $s = \gamma - i\infty$ and traverses clockwise to $s = -\infty$; along this segment the integrands vanish. The contour then continues along the negative side of the branch cut, circles the branch point at zero (counterclockwise), and then extends back along the positive side of the branch cut to $s = -\infty$; numerical integrations are performed along these segments. The contour then circles clockwise around to $s = \gamma + i\infty$, with the integrands vanishing again along this segment. The difference between the integrals over this contour and those defined by equation (A2) is then simply equal to minus the sum of the residues at any off-axis poles. There are no poles at the nominal film thickness, however at larger film thickness poles do appear, first in a single pair and then with multiple pairs, as thickness increases further.

[52] A MATLAB code was used to calculate the pore pressure and temperature from the expressions in equation (A2). The QUAD integration routine was used to evaluate the integrals over the different components of the integration path described above. Along the negative real axis the integrals were split into separate large and small $|s|$ components, with the division chosen at a value of s such that $sh^2/\alpha_{th} \ll 1$. The integrands in (A2) were approximated to first order in sh^2/α_{th} for both the small $|s|$ integrals on the negative real axis, and the integrals around the branch point at zero. The fault strength and fracture energy were determined subsequently, with the latter calculated from the results for pore pressure as a function of slip distance, using a compound trapezoid rule at logarithmically spaced points to evaluate equation (9).

[53] The same procedure can be followed for the general case in which the thermal and hydraulic diffusivities change discontinuously at the shear boundary. The required steps are straightforward. However, the resulting formulas are cumbersome and we do not present them here.

Appendix B: Gaussian Shear Distribution

[54] Here the formulation is given of the integral equation, and the Laplace transform of its solution, for shear rate in the form of the *Andrews* [2002] Gaussian distribution, as given in equation (15). Further, the approximation is made that although the entire layer shears, the constitutive relation is based on the highest pore pressure, presumed to be at the layer center $y = 0$, which, as remarked by *Rice* [2006], is not consistent with having distributed shear. Thus its thickness scale w will be regarded as some microstructurally demanded thickness, in recognition that slip on a mathe-

matal plane is not a physical possibility in a granular aggregate. Thus, using equation (1) to describe the strength as $\tau(t) = f(t)[\sigma_n - P(0, t)]$, the integral equation analogous to that given by Rice [2006] for deriving the result presented in section 3.2 for slip on a plane, is

$$P(0, t) = P_0 + \frac{\Lambda}{\sqrt{2\pi}(\alpha_{hy} - \alpha_{th})\rho c} \int_0^t \left[\frac{\alpha_{hy}\tau(t')V(t')}{\sqrt{w^2 + 2\alpha_{hy}(t-t')}} - \frac{\alpha_{th}\tau(t')V(t')}{\sqrt{w^2 + 2\alpha_{th}(t-t')}} \right] dt'.$$

The temperature rise at the center of the shearing layer is

$$T(0, t) = T_{amb} + \frac{1}{\sqrt{2\pi}\rho c} \int_0^t \frac{\tau(t')V(t')}{\sqrt{w^2 + 2\alpha_{th}(t-t')}} dt'.$$

[55] Consider now the special case of f and V that are constant in time. Having discovered the utility of L^* , the resulting strength is written $\tau = \tau(D)$ where $D = \delta/L^* = Vt/L^*$. Then defining $W_{hy} = w/\sqrt{2\alpha_{hy}L^*/V}$ and $W_{th} = w/\sqrt{2\alpha_{th}L^*/V}$, and now defining the Laplace transform by $\hat{\tau}(S) = \int_0^\infty \tau(D)\exp(-SD) dD$, the integral equation transforms to

$$\frac{f(\sigma_n - P_0)}{S} - \hat{\tau}(S) = \frac{\hat{\tau}(S)Q(S)}{\sqrt{S}},$$

where

$$Q(S) = \frac{\sqrt{\alpha_{hy}} \exp(W_{hy}^2 S) \operatorname{erfc}(W_{hy}\sqrt{S}) - \sqrt{\alpha_{th}} \exp(W_{th}^2 S) \operatorname{erfc}(W_{th}\sqrt{S})}{\sqrt{\alpha_{hy}} - \sqrt{\alpha_{th}}},$$

and it has been recognized that $\exp(W^2 S)\operatorname{erfc}(W\sqrt{S})\sqrt{\pi/S}$ is the transform of $1/\sqrt{W^2 + D}$. Thus the transform of the solution $\tau = \tau(D)$ is

$$\hat{\tau}(S) = \frac{f(\sigma_n - P_0)}{[Q(S) + \sqrt{S}]\sqrt{S}}.$$

[56] This agrees with the result for slip on a plane, as it should, when $w = 0$ ($\rightarrow W_{hy} = W_{th} = 0$). The inversion integral can be set up like for that case of slip on a plane, assuming as is valid in that case, that we can distort the inversion integration contour without crossing singularities so that it wraps around the entire negative S axis. Writing $S = u^2 \exp(\pm i\pi)$ (with u real and ≥ 0) to denote points on the two sides of that axis, and noting that

$$\exp(W^2 u^2 e^{\pm i\pi}) \operatorname{erfc}(Wu e^{\pm i\pi/2}) = \exp(-W^2 u^2) \mp \frac{2iW}{\sqrt{\pi}} \int_0^u \exp[-W^2(u^2 - v^2)] dv,$$

there results

$$\tau(\delta) = \frac{2}{\pi} f(\sigma_n - P_0) \int_0^\infty \frac{A(u) \exp(-u^2 \delta/L^*)}{A^2(u) + B^2(u)} du,$$

where

$$A(u) = \frac{\sqrt{\alpha_{hy}} \exp(-W_{hy}^2 u^2) - \sqrt{\alpha_{th}} \exp(-W_{th}^2 u^2)}{\sqrt{\alpha_{hy}} - \sqrt{\alpha_{th}}},$$

and

$$B(u) = u - \frac{2/\sqrt{\pi}}{\sqrt{\alpha_{hy}} - \sqrt{\alpha_{th}}} \left[W_{hy} \sqrt{\alpha_{hy}} \int_0^u \exp(-W_{hy}^2(u^2 - v^2)) dv - W_{th} \sqrt{\alpha_{th}} \int_0^u \exp(-W_{th}^2(u^2 - v^2)) dv \right].$$

Also, the fracture energy associated with this formulation is

$$G(\delta) = \frac{2}{\pi} f(\sigma_n - P_0) L^* \int_0^\infty \frac{A(u)[1 - (1 + u^2 \delta/L^*) \exp(-u^2 \delta/L^*)]}{[A^2(u) + B^2(u)]u^2} du.$$

It can be seen at this point that the complete symmetry of the dependence of the slip-weakening relation on the diffusivities is retained in this model as well.

[57] The temperature rise at $y = 0$ can be determined too, but it has no simple relation to the pressure rise and strength drop like for the model of slip on a plane. Writing $\Delta T(D) = T(0, t) - T_{amb}$, transforming the expression above for $\Delta T(D)$, gives

$$\begin{aligned} \Delta \hat{T}(S) &= \frac{1}{2\sqrt{S}\rho c} \sqrt{\frac{VL^*}{\alpha_{th}}} \hat{\tau}(S) \exp(W_{th}^2 S) \operatorname{erfc}(W_{th}\sqrt{S}), \\ &= \frac{f}{2} \sqrt{\frac{VL^*}{\alpha_{th}}} \frac{\sigma_n - P_0}{\rho c} \frac{\exp(W_{th}^2 S) \operatorname{erfc}(W_{th}\sqrt{S})}{[Q(S) + \sqrt{S}]S}, \end{aligned}$$

which must be inverted in a manner similar to what is done above for the strength versus slip relation. We note that the possible maximum temperature rise predicted by this model is

$$\begin{aligned} T_{max} - T_{amb} &= \lim_{D \rightarrow \infty} \Delta T(D) = \lim_{S \rightarrow \infty} [S \Delta \hat{T}(S)] \\ &= \frac{f}{2} \sqrt{\frac{VL^*}{\alpha_{th}}} \frac{\sigma_n - P_0}{\rho c}. \end{aligned}$$

[58] That is the very same result as for the case of slip on a plane although we must generally expect the temperature rise at any finite amount of slip to be lower than for that planar case. The limit is for unbounded slip, which requires unbounded time, and hence assures that diffusion penetration distances like $\sqrt{w^2 + 2\alpha t}$ have become arbitrarily large compared to any fixed w .

Appendix C: State-Dependent Property Formulation

[59] To account for the dependence of fault zone properties on the pressure and temperature state, a term of the form

$$\frac{1}{\rho c} \frac{\partial T}{\partial y} \frac{\partial}{\partial y} (\rho c \alpha_{th})$$

was added to the right sides of equations (3) and (4), and a term of the form

$$\frac{1}{\beta} \frac{\partial P}{\partial y} \frac{\partial}{\partial y} (\beta \alpha_{hy})$$

was added to the right sides of equations (6) and (7). The resulting system of equations was solved using the method of lines with a second-order finite difference spatial discretization and constant step size. The MATLAB stiff ordinary differential equation packages were used subsequently to solve for the state evolution. Far-field zero flux boundary conditions were implemented.

[60] Property values were updated at each time step using the same scheme of interpolations, extrapolations, and curve fits described for the depth-dependent calculations shown in Figures 11 to 13. The exception is the permeability values, which are still based on data from *Wibberley* [2002, also private communication, 2003], as well as *Wibberley and Shimamoto* [2003], however for this set of calculations the measurements made on unloading the laboratory samples are considered more appropriate. In particular, we performed an exponential fit to the subset of data reported in Table 1 of *Rice* [2006] and used that formula in the numerical scheme described above. This procedure served as the basis for obtaining the values reported in columns 3, 4, 6, and 7 of Table 1.

[61] The calculations shown in Figures 14–17 were performed at 601 equally spaced nodes, 5 of which were within the shear zone.

[62] **Acknowledgments.** Support is gratefully acknowledged to NSF grants EAR-0125709 and 0510193 and to the NSF/USGS Southern California Earthquake Center (SCEC), funded by NSF Cooperative Agreement EAR-0106924 and USGS Cooperative Agreement 02HQAG0008. This is SCEC contribution 1003. We are grateful to D. Garagash and an anonymous reviewer for helpful comments.

References

- Abercrombie, R. E., and J. R. Rice (2005), Can observations of earthquake scaling constrain slip weakening?, *Geophys. J. Int.*, *162*, 406–424, doi:10.1111/j.1365-246X.2005.02579.x.
- Andrews, D. J. (2002), A fault constitutive relation accounting for thermal pressurization of pore fluid, *J. Geophys. Res.*, *107*(B12), 2363, doi:10.1029/2002JB001942.
- Bowden, F. P., and P. H. Thomas (1954), The surface temperature of sliding solids, *Proc. R. Soc. London, Ser. A*, *223*, 29–40.
- Burnham, C. W., J. R. Holloway, and N. F. Davis (1969), Thermodynamic properties of water to 1000°C and 10,000 bars, *Spec. Pap. Geol. Soc. Am.*, *132*, 96 pp.
- Chester, F. M., and J. S. Chester (1998), Ultracataclastic structure and friction processes of the Punchbowl fault, San Andreas system, California, *Tectonophysics*, *295*, 199–221.
- Chester, J. S., and D. L. Goldsby (2003), Microscale characterization of natural and experimental slip surfaces relevant to earthquake mechanics, *Annu. Prog. Rep. 2003*, South. Calif. Earthquake Cent., Los Angeles.
- Chester, J. S., A. K. Kronenberg, F. M. Chester, and R. N. Guillemette (2003), Characterization of natural slip surfaces relevant to earthquake mechanics, *Eos Trans. AGU*, *84*(46), Fall Meet. Suppl., Abstract S42C-0185.
- Chester, F. M., J. S. Chester, D. L. Kirschner, S. E. Schulz, and J. P. Evans (2004), Structure of large-displacement strike-slip fault zones in the brittle continental crust, in *Rheology and Deformation in the Lithosphere at Continental Margins*, edited by G. D. Karner et al., pp. 223–260, Columbia Univ. Press, New York.
- Chester, J. S., F. M. Chester, and A. K. Kronenberg (2005), Fracture surface energy of the Punchbowl Fault, San Andreas System, *Nature*, *437*, 133–136.
- Di Toro, G., D. L. Goldsby, and T. E. Tullis (2004), Friction falls towards zero in quartz rock as slip velocity approaches seismic rates, *Nature*, *427*, 436–460.
- Goldsby, D. L., and T. E. Tullis (2002), Low frictional strength of quartz rocks at subseismic slip rates, *Geophys. Res. Lett.*, *29*(17), 1844, doi:10.1029/2002GL015240.
- Heaton, T. H. (1990), Evidence for and implications of self-healing pulses of slip in earthquake rupture, *Phys. Earth Planet. Inter.*, *64*, 1–20.
- Hirose, T., and T. Shimamoto (2005), Growth of a molten zone as a mechanism of slip weakening of simulated faults in gabbro during frictional melting, *J. Geophys. Res.*, *110*(B5), B05202, doi:10.1029/2004JB003207.
- Jeffreys, H. (1942), On the mechanics of faulting, *Geol. Mag.*, *79*, 291–295.
- Keenan, J. H., F. G. Keyes, P. G. Hill, and J. G. Moore (1978), *Steam Tables*, 156 pp., John Wiley, Hoboken, N. J.
- Lachenbruch, A. H. (1980), Frictional heating, fluid pressure and the resistance to fault motion, *J. Geophys. Res.*, *85*, 6097–6112.
- Lachenbruch, A. H., and J. H. Sass (1980), Heat flow and energetics of the San Andreas fault zone, *J. Geophys. Res.*, *85*, 6185–6222.
- Lockner, D., H. Naka, H. Tanaka, H. Ito, and R. Ikeda (2000), Permeability and strength of core samples from the Nojima fault of the 1995 Kobe earthquake, in *Proceedings of the International Workshop on the Nojima Fault Core and Borehole Data Analysis*, Tsukuba, Japan, Nov 22–23, 1999, edited by H. Ito et al., *U.S. Geol. Surv. Open File Rep.*, *00-129*, 147–152.
- Mase, C. W., and L. Smith (1985), Pore-fluid pressures and frictional heating on a fault surface, *Pure Appl. Geophys.*, *122*, 583–607.
- Mase, C. W., and L. Smith (1987), Effects of frictional heating on the thermal, hydrologic, and mechanical response of a fault, *J. Geophys. Res.*, *92*, 6249–6272.
- McKenzie, D. P., and J. N. Brune (1972), Melting on fault planes during large earthquakes, *Geophys. J. R. Astron. Soc.*, *29*, 65–78.
- Noda, H., and T. Shimamoto (2005), Thermal pressurization and slip-weakening distance of a fault: An example of the Hanaore fault, southwest Japan, *Bull. Seismol. Soc. Am.*, *95*, 1224–1233.
- Poliakov, A. N. B., R. Dmowska, and J. R. Rice (2002), Dynamic shear rupture interactions with fault bends and off-axis secondary faulting, *J. Geophys. Res.*, *107*(B11), 2295, doi:10.1029/2001JB000572.
- Prakash, V. (2004), Pilot studies to determine the feasibility of using new experimental techniques to measure sliding resistance at seismic slip rates, *Annu. Prog. Rep. 2004*, South. Calif. Earthquake Cent., Los Angeles.
- Prakash, V., and F. Yuan (2004), Results of a pilot study to investigate the feasibility of using new experimental techniques to measure sliding resistance at seismic slip rates, *Eos Trans. AGU*, *85*(47), Fall Meet. Suppl., Abstract T21D-02.
- Rice, J. R. (1999), Flash heating at asperity contacts and rate-dependent friction, *Eos Trans. AGU*, *84*(46), Fall Meet. Suppl., Abstract S41G-01.
- Rice, J. R. (2006), Heating and weakening of faults during earthquake slip, *J. Geophys. Res.*, *111*, B05311, doi:10.1029/2005JB004006.
- Rice, J. R., and M. Cocco (2006), Seismic fault rheology and earthquake dynamics, in *The Dynamics of Fault Zones*, edited by M. R. Handy, MIT Press, Cambridge, Mass., in press.
- Rice, J. R., J. W. Rudnicki, and V. C. Tsai (2005), Shear localization in fluid-saturated fault gouge by instability of spatially uniform, adiabatic, undrained shear, *Eos Trans. AGU*, *86*(52), Fall Meet. Suppl., Abstract T13E-05.
- Roig Silva, C., D. L. Goldsby, G. Di Toro, and T. E. Tullis (2004), The role of silica content in dynamic fault weakening due to gel lubrication, *Eos Trans. AGU*, *85*(47), Fall Meet. Suppl., Abstract T21D-06.
- Rowe, C. D., J. C. Moore, F. Meneghini, and A. W. McKeirnan (2005), Large-scale pseudotachylytes and fluidized cataclases from an ancient subduction thrust fault, *Geology*, *33*(12), 937–940.
- Segall, P., and J. R. Rice (1995), Dilatancy, compaction, and slip instability of a fluid-infiltrated fault, *J. Geophys. Res.*, *100*, 22,155–22,171.
- Sibson, R. H. (1973), Interactions between temperature and pore-fluid pressure during earthquake faulting and a mechanism for partial or total stress relief, *Nature*, *243*, 66–68.
- Sibson, R. H. (2003), Thickness of the seismic slip zone, *Bull. Seismol. Soc. Am.*, *93*, 1169–1178.
- Sibson, R. H., and V. Toy (2006), The habitat of fault-generated pseudotachylyte: Presence vs. absence of friction melt, in *Radiated Energy and the Physics of Earthquake Faulting*, *Geophys. Monogr. Ser.*, edited by R. Abercrombie, A. McGarr, H. Kanamori, and G. DiToro, AGU, Washington, D. C., in press.
- Tödheide, K. (1972), Water at high temperatures and pressures, in *Water: A Comprehensive Treatise*, vol. 1, *The Physics and Physical Chemistry of Water*, edited by F. Franks, pp. 463–514, Springer, New York.
- Tsutsumi, A., and T. Shimamoto (1997), High-velocity frictional properties of gabbro, *Geophys. Res. Lett.*, *24*, 699–702.
- Tullis, T. E., and D. L. Goldsby (2003a), Flash melting of crustal rocks at almost seismic slip rates, *Eos Trans. AGU*, *84*(46), Fall Meet. Suppl., Abstract S51B-05.

- Tullis, T. E., and D. L. Goldsby (2003b), Laboratory experiments on fault shear resistance relevant to coseismic earthquake slip, *Annu. Prog. Rep. 2003*, South. Calif. Earthquake Cent., Los Angeles.
- Vosteen, H.-D., and R. Schellschmidt (2003), Influence of temperature on thermal conductivity, thermal capacity and thermal diffusivity for different types of rock, *Phys. Chem. Earth*, 28, 499–509.
- Wibberley, C. A. J. (2002), Hydraulic diffusivity of fault gouge zones and implications for thermal pressurization during seismic slip, *Earth Planets Space*, 54(11), 1153–1171.
- Wibberley, C. A. J., and T. Shimamoto (2003), Internal structure and permeability of major strike-slip fault zones: The Median Tectonic Line in Mie Prefecture, southwest Japan, *J. Struct. Geol.*, 25, 59–78.
- Wibberley, C. A. J., and T. Shimamoto (2005), Earthquake slip weakening and asperities explained by thermal pressurization, *Nature*, 436, 689–692.

A. W. Rempel, Department of Geological Sciences, University of Oregon, Eugene, OR 97403, USA. (rempe@uoregon.edu)

J. R. Rice, Department of Geological Sciences, University of Oregon, 224 Pierce Hall, 29 Oxford St., Cambridge, MA 02138-0000, USA.